Journal of Volcanology and Geothermal Research xxx (2009) xxx–xxx

Contents lists available at ScienceDirect

Journal of Volcanology and Geothermal Research

journal homepage: www.elsevier.com/locate/jvolgeores

Compositional evolution of magma from Parícutin Volcano, Mexico: The tephra record

E.J. Erlund [a], K.V. Cashman [a,*], P.J. Wallace [a], L. Pioli [a,b], M. Rosi [c], E. Johnson [a,d], H. Delgado Granados [e]

[a] Department of Geological Sciences, University of Oregon, Eugene, OR, USA
[b] Department of Mineralogy, University of Geneva, Geneva, Switzerland
[c] Dipartimento di Scienze della Terra, Universitá di Pisa, Pisa, Italy
[d] CODES, University of Tasmania, Hobart, Tasmania, Australia
[e] Instituto de Geofísica, UNAM, Ciudad Universitaria, 04510 México, D.F., Mexico

ARTICLE INFO

Available online xxxx

Keywords:
scoria cone
violent Strombolian
tephra
magma evolution
Paricutin

ABSTRACT

The birth of Parícutin Volcano, Mexico, in 1943 provides an unprecedented opportunity to document the development of a monogenetic cinder cone and its associated lava flows and tephra blanket. Three 'type' sections provide a complete tephra record for the eruption, which is placed in a temporal framework by comparing both bulk tephra and olivine phenocryst compositions to dated samples of lava and tephra. Our data support the hypothesis of Luhr (2001) that the first four months of activity were fed by a magma batch (Phase 1) that was distinct from the magma that supplied the subsequent eight years of activity. We further suggest that the earliest erupted (vanguard) magma records evidence of temporary residence at shallow levels prior to eruption, suggesting early development of a dike and sill complex beneath the vent. Depletion of this early batch led to diminished eruptive activity in June and July of 1943, while arrival of the second magma batch (Phase 2) reinvigorated activity in late July. Phase 2 fed explosive activity from mid-1943 through 1946, although most of the tephra was deposited by the end of 1945. Phase 3 of the eruption began in mid-1947 with rapid evolution of magma compositions from basaltic andesite to andesite and dominance of lava effusion. The combined physical and chemical characteristics of the erupted material present a new interpretation of the physical conditions that led to compositional evolution of the magma. We believe that syn-eruptive assimilation of wall rock in a shallow complex of dikes and sills is more likely than pre-eruptive assimilation within a large magma chamber, as previously assumed. We further suggest that waning rates of magma supply from the deep feeder system allowed evolved, shallowly stored magma to enter the conduit in 1947, thus triggering the rapid observed change in the erupted magma composition. This physical model predicts that assimilation should be observable in other monogenetic eruptions, particularly those with low pressure melt inclusions and with eruption durations of months to years.

1. Introduction

Cinder cones are the most common volcanic landform on Earth. Cinder cone fields commonly contain hundreds of individual vents, many of which have associated lava flows. Individual cones and associated flows and tephra blankets are assumed to be monogenetic, formed during a single eruptive episode from the ascent and eruption of a single magma batch. However, detailed studies indicate that some eruptions are fed by multiple magma batches (e.g., Strong and Wolff, 2003; Cervantes and Wallace, 2003a; Johnson et al., 2008), that individual magma batches may evolve through both fractionation and assimilation (e.g., Wilcox, 1954; McBirney et al., 1987; Johnson et al., 2008), and that some cones are re-occupied, feeding multiple eruptions over decades to centuries (McKnight and Williams, 1997). Also variable are the styles of activity that comprise a single eruptive episode, which may include Hawaiian, Strombolian, violent Strombolian, Vulcanian and purely effusive phases (e.g., Valentine et al., 2006; Valentine et al., 2007; Valentine and Gregg, 2008). The combined evidence for multiple magma batches and variations in eruptive style raises questions about the extent to which the nature of the physical activity reflects changes in both deep- and shallow-sourced variations in magma supply rate or composition.

The link between physical and compositional characteristics is of particular interest in determining the origin of violent Strombolian eruptions, perhaps the most distinctive of all of the forms of eruptive activity associated with cinder cone fields. The term violent Strombolian was introduced by Macdonald (1972) to describe the energetic 'cineritic' phase of Parícutin's activity, which involved strongly pulsatory explosions of moderate size (eruption columns ≤7–8 km high) and simultaneous lava effusion from lateral vents (typically located either within or at the base of the cinder cone). This type of activity appears to

* Corresponding author.
E-mail address: cashman@uoregon.edu (K.V. Cashman).

0377-0273/$ – see front matter © 2009 Elsevier B.V. All rights reserved.
doi:10.1016/j.jvolgeores.2009.09.015

be characteristic of mafic eruptions when mass eruption rates are ~10^5 kg/s and the magma is sufficiently hydrous to produce separated flow conditions in the conduit (e.g., Pioli et al., 2008, 2009). However, although the high H_2O content of mafic subduction zone and intraplate magmas is now broadly recognized (e.g., Roggensack et al., 1997; Nicholis and Rutherford, 2004; Spilliaert et al., 2006; Johnson et al., 2008; Pioli et al., 2008), the extent to which magmatic vs. phreatic water is responsible for both eruptive vigor and extensive ash production accompanying violent Strombolian activity remains a topic of debate (e.g., Valentine et al., 2005; Martin and Nemeth, 2006).

The 1943–1952 eruption of Parícutin is the type example of a violent Strombolian eruption. For volcanologists, the abundance of tephra produced by the eruption (~2/3 of the total mass erupted), the strength of the tephra-producing explosions, and the fine average grain size of the tephra deposit have become defining characteristics of this eruptive style. For petrologists, Parícutin provided one of the first well-documented examples of assimilation (Wilcox, 1954). For these reasons, we have returned to Parícutin to re-examine both the physical volcanology of the eruption (Pioli et al., 2008) and the magma evolution through a compositional and textural study of the pyroclastic deposits (this study). We demonstrate that: (1) early tephra samples provide important clues to the nature of the initial magma that are not preserved in the classic lava flow samples from this eruption (e.g., Wilcox, 1954; McBirney et al., 1987); (2) the tephra records all of the bulk geochemical changes present in the lava flow sequence, thus providing a detailed view of both deep and shallow magmatic processes (e.g., Johnson et al., 2008, this volume; (3) combined evidence of shallow (<100 MPa) magma storage and early melting of granite basement support a model of syn-eruptive crustal assimilation within a shallow magma storage system; and (4) preserved relationships among magma eruption rate, compositional change, and eruptive style provide insight into both the longevity of individual cinder cone eruptions and the range of activity observed at volcanoes of basaltic andesite composition (including current activity at Kluchevskoy, Llaima, and Tungurahua).

2. Background

2.1. Geological setting of Parícutin volcano, Mexico

Parícutin is located in the Michoacán-Guanajuato Volcanic Field (MGVF) of the Trans-Mexican Volcanic Belt (TMVB), which trends east–west across Mexico. Volcanism in the TMVB is related to subduction of the Cocos and Rivera Plates beneath Mexico at the Middle America Trench (Fig. 1). The MGVF is made up of about 1000 small eruptive vents and 378 medium-sized volcanoes over a 40,000-km^2 area (Hasenaka, 1994). The medium-sized volcanoes are dominantly shield volcanoes (Hasenaka et al., 1994), whereas about 90% of the small vents are cinder cones (Hasenaka and Carmichael, 1985a,b). There have been only two historic eruptions, those of Parícutin (mid 20th century) and Jorullo (late 18th century), both of which produced relatively long-lived cinder cones (9 yr and 15 yr, respectively).

Monogenetic centers in the MGVF are composed primarily of calc-alkaline basalt and basaltic andesite (Hasenaka and Carmichael, 1987). As the cinder cones show evidence for only limited fractional crystallization (~23% at Jorullo; Luhr and Carmichael, 1985) and are active for only short periods of time (months to years), it has been inferred that they do not develop long-lived magma chambers (Hasenaka and Carmichael, 1985a) and that primitive compositions at cinder cones represent near-primary mantle melts (e.g. Cervantes and Wallace, 2003b; Johnson et al., in press).

2.2. The 1943–1952 Parícutin eruption

The eruption of Parícutin began on 20th February 1943 after about 45 days of precursory seismicity (Yokoyama and De la Cruz-Reyna, 1990); it ended almost exactly nine years later. Notable features of the eruption include a progressive decrease in average mass eruption rate and corresponding increase in the importance of effusive (relative to explosive) activity, a change in bulk magma composition from basaltic andesite to andesite over the course of the eruption, and eruption styles

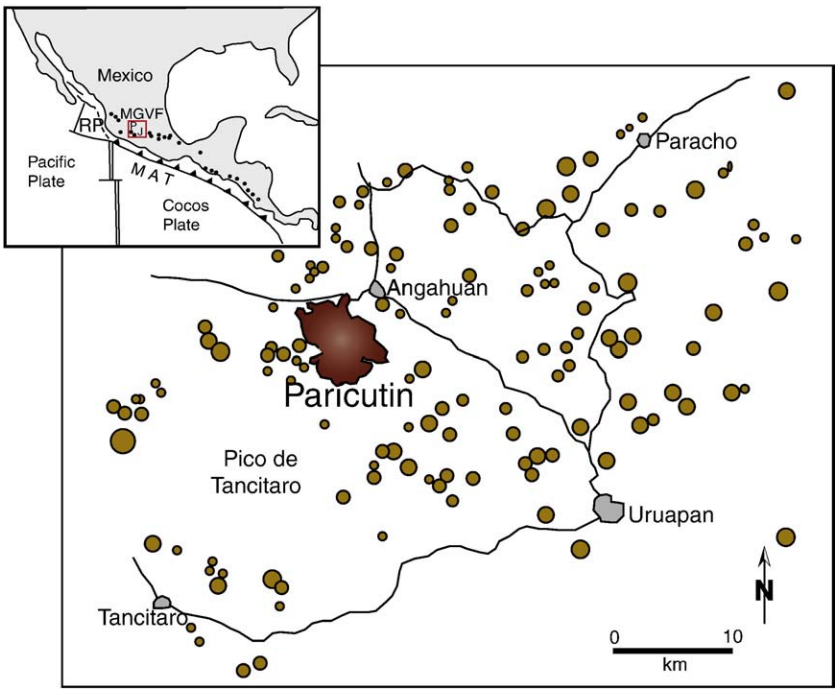

Fig. 1. Sketch map of the Parícutin region showing the distribution of young cinder cones (modified from McBirney et al., 1987). All of the vents produced basalt or basaltic andesite magma (Hasenaka and Carmichael, 1987). Pico de Tancítaro is an eroded stratovolcano that was active from 237 to >793 ka (Ownby et al., 2007). Inset shows the location of the Michoacan-Guanajuato Volcanic Field (MGVF) within the Trans-Mexican Volcanic Belt and the associated plate tectonic configuration. RP = Rivera Plate; MAT = Middle America Trench. Volcanoes are shown by small dots. P = Parícutin; J = Jorullo.

Please cite this article as: Erlund, E.J., et al., Compositional evolution of magma from Parícutin Volcano, Mexico: The tephra record, Journal of Volcanology and Geothermal Research (2009), doi:10.1016/j.jvolgeores.2009.09.015

ranging from Strombolian to violent Strombolian to Vulcanian, all of which were accompanied by effusive activity. Contemporary accounts (collected and summarized in Luhr and Simkin, 1993) provide detailed observations of changes in eruptive activity through time, from an early cone-building phase (the first month) through an extended violent Strombolian phase (intermittently from mid-1943 through 1945) to the last six years of lava flows punctuated by late-stage Vulcanian explosions. Here we highlight features of that activity that can be directly related to petrologic changes in the eruptive products.

The eruption started at about 4 pm with the formation of a fissure and emergence of "a small simple column that grew little by little; a vapor of strange gray rising silently toward the SE" (Foshag and González-Reyna, 1956). Continuous low-level eruptive activity over the next three weeks produced a horseshoe-shaped cinder cone, lava flows, and an eruption column bent toward the southwest, toward the stratovolcano Tancitaro (Fig. 1). A period of intense explosive activity from mid-March to early June 1943 generated eruption columns to ≤8 km above the crater rim, substantial ash fall in Uruapan, and ash deposition as far away as Mexico City, 320 km to the east (Fries, 1953). The activity became more erratic after June, but strong 'cineritic' behavior resumed in late July and lasted until mid-October. Initiation of a new effusive vent to the NE (the Sapichu vent) caused activity at the main vent to cease, thus ending the 'Quitzocho' phase of the eruption.

The 'Sapichu' eruptive phase lasted only 2.5 months and was primarily effusive. However, activity during this phase also produced highly vesicular tephra and occasional bombs cored by partially fused granite xenoliths. Both features led Krauskopf (1948) to infer that the dike feeding this phase originated at some depth below the main cone.

Explosive activity in the main vent resumed after the Sapichu period but with decreasing frequency. Fries (1953) estimated that approximately 46% of the total pyroclastic material (tephra + cone) was erupted in 1943, and almost 80% had erupted by the end of 1945 (Fig. 2A), as documented by the similarity of isopach maps produced in May 1945 (Krauskopf and Williams, 1946) and in late 1946 (Segerstrom, 1950). During the last six years of the eruption, tephra volumes were negligible in comparison to lava volumes (Fries, 1953). Vulcanian activity began in 1949, increased in intensity in mid-1951, and ended abruptly on 25th February 1952, when cessation of both lava emission and crater activity ended the nine-year eruption.

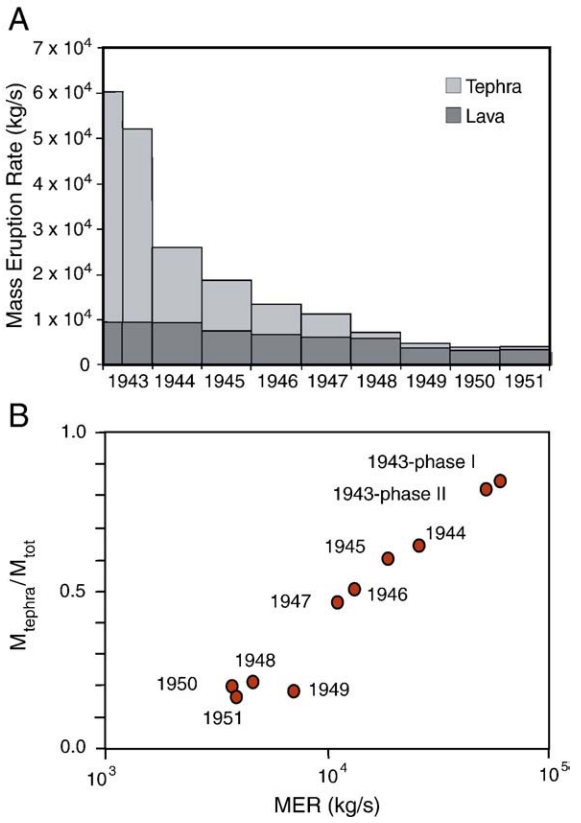

Fig. 2. Temporal changes in eruptive products. (A) Variations in mass eruption rates of tephra and lava throughout the eruption (modified from Fries, 1953). Rates are annual averages except for 1943, where contributions from Phase 1 and Phase 2 magmas are calculated separately (see Pioli et al., 2008). (B) Data from (A) replotted to show changes in the mass fraction of tephra (relative to tephra + cone + lava) as a function of total mass eruption rate (from Pioli et al., 2008).

2.3. Physical volcanology

Detailed maps of both tephra and lava distribution were made throughout the eruption (Luhr and Simkin, 1993). These measurements chronicle the decrease in the relative volume flux of tephra and lava through time (Fig. 2) and provide a detailed look at the growth of a basaltic andesite flow field. Pioli et al. (2008) re-examined key tephra sections to tie deposit characteristics to contemporary accounts, with the goal of developing a more robust definition of violent Strombolian activity. In the field, we found the most striking characteristic of the tephra deposits to be the fine-scale (typically centimeters) alternation between ash and lapilli beds, a dramatic testimony to the pulsatory nature of this eruption style that is well chronicled in eyewitness accounts.

Krauskopf (1948) interpreted the dual explosive and effusive activity to reflect gas segregation at the base of the cone, such that gas-rich magma accelerates upward to cause explosions while the remaining, gas-poor magma travels laterally to produce lava flows. Pioli et al. (2008) showed that these data demonstrate changes in the efficiency of gas segregation at different mass eruption rates, with higher mass eruption rates producing a higher proportion of tephra relative to lava (Fig. 2B). This behavior can be modelled by considering separated flow conditions at a T-junction (Pioli et al., 2009), which determines the relative proportion of gas segregation into the vertical (tephra-producing) and horizontal (lava-producing) conduits. Together the observational data and model demonstrate that segregation of gas and magma is most efficient at mass eruption rates ~10^4–10^5 kg/s, consistent with observed conditions for violent Strombolian activity at Parícutin.

2.4. Petrologic studies

Most (~80%) of the Parícutin magma is basaltic andesite with 2–3% phenocrystic olivine and microphenocrysts (and microlites) of plagioclase, olivine, orthopyroxene and clinopyroxene (Wilcox, 1954). Early (February 22, 1943) and late (1950, 1952) lavas also contain minor phenocrystic plagioclase. The bulk composition of the magma evolved from basaltic andesite to andesite in 1947 (Fig. 3), producing a change in the phenocryst assemblage from olivine to orthopyroxene. A classic study by Wilcox (1954) demonstrated that this compositional change was best explained by fractionation accompanied by assimilation of granitic country rock. This interpretation was confirmed by McBirney et al.'s (1987) isotopic study of the same samples. Both studies assumed that the assimilation occurred prior to the eruption, and that pre-eruptive magma resided in a single magma reservoir that was zoned in composition.

Luhr (2001) demonstrated that the dramatic compositional change in 1947 was only part of the petrologic story. His study of olivine-hosted melt inclusions suggests an additional shift in magma composition between June and August of 1943, as bracketed by contrasting K_2O contents of early erupted material (lava samples from February 22 and March, 1943, and a tephra sample collected on May 26, 1943) and all subsequent basaltic andesite samples. On the basis of this compositional change, Luhr (2001) divided the eruption into three phases: Phase 1 lasted from February to July (?) 1943 and was characterized by bulk $K_2O < 1$ wt.%; Phase 2 had commenced by

Please cite this article as: Erlund, E.J., et al., Compositional evolution of magma from Parícutin Volcano, Mexico: The tephra record, Journal of Volcanology and Geothermal Research (2009), doi:10.1016/j.jvolgeores.2009.09.015

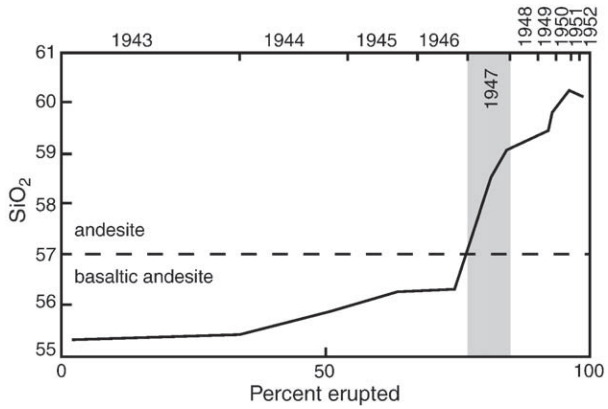

Fig. 3. Changes in bulk magma composition through the eruption, normalized to the total volume of lava erupted. Redrafted from McBirney et al. (1987).

August 1, 1943, continued through 1946, and was characterized by K_2O ~1.2 wt.%; and Phase 3 spanned the final six years of the eruption (late 1946–1952), when bulk SiO_2 increased from 56.1 to 60.3 wt.% and K_2O increased from 1.2 to 1.7 wt.% (Fig. 3).

Melt inclusion studies (Luhr, 2001; Pioli et al., 2008; Johnson et al., in press) demonstrate that the magma that fed the Paricutin eruption was H_2O-rich (≤4.2 wt.% H_2O). Samples from Phase I and the early part of Phase 2 also contain some melt inclusions that preserve CO_2 (≤1000 ppm), yielding maximum pressures of 370 MPa and estimated trapping depths of ≤14 km. Magmas erupted at nearby Jorullo volcano, the second youngest volcano in the MGVF, also contain high H_2O (≤5.3 wt.%) and CO_2 (≤1000 ppm) contents (Johnson et al., 2008), illustrating that both high volatile contents and mid- to lower crustal sources are common in MGVF monogenetic cones.

2.5. Summary and remaining questions

The work summarized above describes an eruption that was complex in both the physical nature of the activity and the compositional variations of the magma responsible for that activity. Here we attempt to bridge physical (e.g., Fries, 1953; Pioli et al., 2008) and petrologic (Wilcox, 1954; McBirney et al., 1987; Luhr, 2001) studies of the eruption by examining compositional variations through the tephra sections described by Pioli et al. (2008). Our primary goal is to explore links between the eruption dynamics and the compositional evolution of the magma. To do this, we first link the tephra deposit to the (dominantly lava) chronology provided by Wilcox (1954) and Luhr (2001). We then use the tephra to expand Luhr's (2001) petrologic analysis, particularly for the tephra-dominated activity of 1943 and 1944, and to explore links between the evolution of the magma petrology and eruptive style. Finally, we address the physical conditions that may have promoted crustal assimilation.

3. Methods

3.1. Field investigations

Pioli et al. (2008) sampled and characterized tephra deposits from four locations that were chosen to encompass the full range of explosive activity at Parícutin, and that we use in our petrologic study (Fig. 4). Sample site A is close to the cone, on top of late 1946 lava flows. This section thus represents tephra accumulated from the start of 1947 onwards and was selected to encompass the compositional change during the last five years of the eruption. Site B, 5.5 m thick and located about 2 km northwest of the cone and just west of the lava flows, was selected to provide a detailed record of the main phase of the eruption. Site C, 6.5 m thick and located ~1.5 km to the southwest of the cone, was chosen to capture the early phase of the eruption. As site C is underlain by soil, capped by a late-stage bomb, and shows no evidence of internal erosion surfaces, this section also provides a complete section of the proximal stratigraphy. Site D provided additional samples of the earliest tephra fall, which was particularly well preserved at this location. Additional sites that were used to examine the deposit are shown in Fig. 4 as bold numbers, which represent the current thickness of the undisturbed tephra section at that location; numbers in brackets represent partial sections (the result of either erosion or deposition on contemporaneous lava flows).

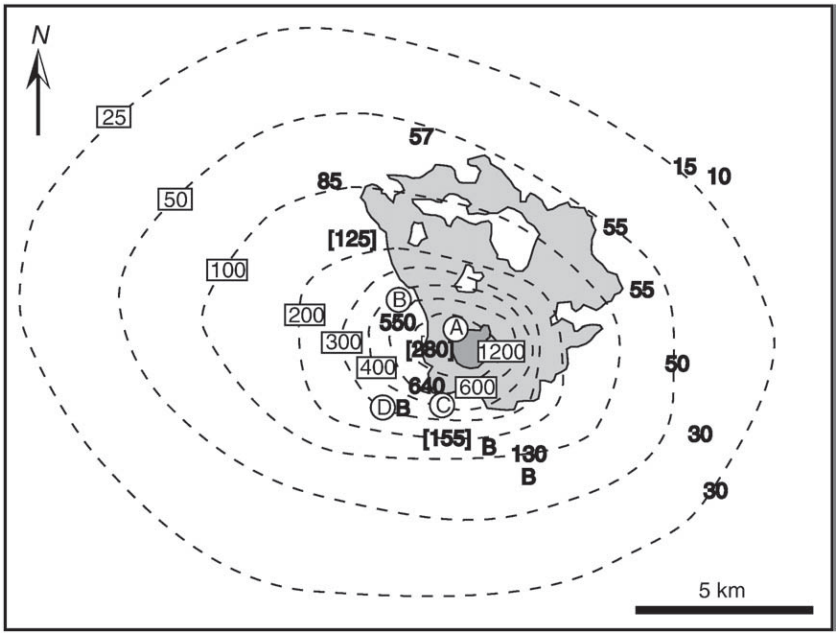

Fig. 4. Map showing locations of field excavations and sampling locations. Current thickness of tephra deposits (in cm) shown in bold, where numbers in brackets denote incomplete sections and B refers to sites excavated only for examination of basal sections. Sampled sections labeled as letters (A, B, C, D). Original isopachs from May 1946 are indicated as dashed lines (data from Segerstrom, 1950). Medium gray shows the extent of lava flows; dark gray shows the location of the scoria cone.

Please cite this article as: Erlund, E.J., et al., Compositional evolution of magma from Parícutin Volcano, Mexico: The tephra record, Journal of Volcanology and Geothermal Research (2009), doi:10.1016/j.jvolgeores.2009.09.015

3.2. Textural analysis

As observed in other violent Strombolian deposits (e.g., Heiken, 1978; Taddeucci et al., 2004; Valentine et al., 2005), individual lapilli beds at Parícutin contain three distinct components: tan, highly vesicular tephra (sideromelane), black scoria (tachylite) and dense fragments (Pioli et al., 2008). To better characterize the components identified in the field we examined clasts selected from throughout the stratigraphic sequence using an FEI QuantaFeg SEM at the University of Oregon in BSE (backscattered imaging) mode (e.g., Blundy and Cashman, 2008). We focus primarily on textural and chemical attributes of the sideromelane, which is least affected by late-stage degassing and crystallization. Selected images were analyzed for vesicularity, crystallinity, and crystal size distributions (CSDs) using the freeware program Image J (http://rsb.info.nih.gov/ij/). Contrasting gray scales for the phases of interest (glass, olivine + pyroxene, plagioclase) allowed automated phase identification. Size distributions were calculated using the average apparent dimension in 2D (that is, √area) as in Cashman et al. (1999).

3.3. Compositional analysis

Major element analysis of tephra included bulk analyses of individual juvenile clasts (by both XRF and EPMA of fused glass beads), analysis of matrix glass, and analysis of loose olivine crystals from selected layers. Bulk data and olivine compositions were presented graphically in Pioli et al. (2008) as a correlation tool only. Here we provide all analytical data (Tables 1, 2 and 3; Appendix Tables A1–A3) and a description of the methods used. Pioli et al. (2008) also show FTIR analyses of olivine-hosted melt inclusions from the basal layer sampled at Site D (their Fig. 4). Analytical data for the melt inclusions (FTIR, EPMA, laser ablation ICP-MS) are given in Johnson et al. (in press).

Table 1
XRF analyses of tan vesicular lapilli.

Sample	PADA-Lo_3b	PADA-Lo_6d	PADA-Lo_11j
Component	tan	tan	tan
Major elements (Weight %)			
SiO_2	55.40	55.66	54.15
TiO_2	0.97	0.98	0.92
Al_2O_3	17.85	17.86	17.81
FeO^T	6.88	6.97	7.06
MnO	0.12	0.12	0.12
MgO	5.20	5.13	5.48
CaO	7.05	7.02	7.26
Na_2O	4.03	4.08	3.95
K_2O	1.12	1.11	0.87
P_2O_5	0.30	0.31	0.27
Sum	98.93	99.25	97.90
Trace elements (ppm)			
Ni	94	93	105
Cr	136	142	148
Sc	19	19	19
V	140	140	150
Ba	354	359	301
Rb	14	13	10
Sr	606	606	599
Zr	131	132	107
Y	19	19	17
Nb	7	7	5
Ga	21	19	17
Cu	36	34	37
Zn	83	83	86
Pb	6	6	6
La	14	16	12
Ce	33	31	26
Th	1	0	1
Nd	19	16	15

Table 2
Three analyses of sample PADA-Lo_6d from a stratigrahic height of 3.36 m at Site B. The first column shows XRF analysis carried out by the GeoAnalytical Laboratory at Washington State University. Labels Bead 1 and Bead 2 represent analyses of melting experiments. Bead 1 was made using the same powder as the XRF analysis and Bead 2 was made from hand-selected clasts. All analyses were recalculated to sum to 100% to facilitate comparison of values.

Oxide	XRF	Bead 1	1σ	Bead 2	1σ
SiO_2	56.09	55.84	(0.25)	56.58	(0.43)
TiO_2	0.989	1.07	(0.05)	0.96	(0.11)
Al_2O_3	17.99	17.93	(0.07)	18.04	(0.07)
FeO	7.02	7.15	(0.19)	7.05	(0.15)
MnO	0.124	0.16	(0.05)	0.12	(0.05)
MgO	5.17	5.33	(0.08)	4.85	(0.09)
CaO	7.07	7.05	(0.15)	7.06	(0.17)
Na_2O	4.11	4.05	(0.20)	3.98	(0.10)
K_2O	1.12	1.12	(0.03)	1.13	(0.03)
P_2O_5	0.313	0.29	(0.01)	0.23	(0.04)
Total	100.00	100.00	$N=10$	100.00	$N=10$

Values in parentheses are 1 standard deviation uncertainties based on 10 analyzed points for each glass.

All bulk analyses used vesicular lapilli clasts handpicked from individual strata. A complete list of samples and analysis types is provided in Table A1. Three of these tephra samples were analyzed by XRF (Table 1) at the GeoAnalytical Laboratory at Washington State University for comparison with whole rock lava data of Wilcox (1954) and calibration of our fused bead technique. The details of XRF analysis, along with its accuracy and precision, are outlined in Johnson et al. (1999). Fused samples were made from ~100 0.5–1-mm clasts of tan scoria that were crushed and fused for 1 h at 1300 °C in a graphite crucible in a Deltec furnace and then drop-quenched in cold water. The resulting glass beads were analyzed on the electron microprobe. Table 2 compares the results of the two bulk analysis methods on a single sample, confirming that the fused bead technique gives bulk compositions within error of the XRF analyses.

Microprobe analyses of fused glass beads (Table 3), matrix glass (Table A2), and loose olivine crystals (Table A3) were performed using a Cameca SX-100 electron microprobe in the Department of Geological Sciences at the University of Oregon. Standards included a combination of natural and artificial glasses and minerals. Glasses were analyzed using an accelerating voltage of 15 kV, 10 nA beam current and, optimally, a 10-μm spot beam diameter, although a 5-μm beam was required to avoid microlites in some highly crystalline clasts. Olivine crystals were analyzed using the same gun voltage but a beam current of 20 nA and beam diameter of 5 μm. Multiple glass analyses of individual lapilli allowed us to assess the variability of matrix glass compositions of single clasts, while analyses of several different lapilli within a given stratigraphic interval provided a measure of variability within a depositional unit. In general, the variability between lapilli is larger than the variability within a single clast.

4. Results

4.1. Field observations

Our field investigations, made >50 years after the end of the eruption, show that excavated tephra sections preserve original depositional textures and deposit thicknesses in most proximal locations (<5 km from the vent; Fig. 4). Even in sections where the uppermost part of the tephra sequence has been disturbed, the basal sequence is often well preserved (Fig. 5A), particularly in areas to the south and west of the cone that received most of the tephra fall during early phases of the eruption (Foshag and González-Reyna, 1956). The lowermost tephra layer is thin (<5 cm) and composed of black scoria and dense black clasts. This is overlain by at least one (and sometimes two) thin (~5 cm) whitish layers that are almost exclusively highly vesicular tan tephra. Both the dense layers and the whitish layers

Please cite this article as: Erlund, E.J., et al., Compositional evolution of magma from Parícutin Volcano, Mexico: The tephra record, Journal of Volcanology and Geothermal Research (2009), doi:10.1016/j.jvolgeores.2009.09.015

Table 3
Electron microprobe analyses of fused glass beads made from handpicked tan vesicular lapilli.

Sample	PADA-Up_B	PADA-Up_H	PADA-Up_Q	PADA-Lo_6d	PADA-Lo_6d_XRF	P-2007-bombC	P-2007_11	P-2007_17	P-2007_19a	P-04-06_2c1	P-04-06_4c	P-2007_3a	P-2007_6a	P-2007_9b	P-2007_10	P-2007_10	P-05-06_3
Component	tan	tan	tan	tan	tan	–	tan	tan	tan	tan	tan	tan	tan	tan	tan	dense	tan
Phase	3	3	3	2	2	3	2	2	2	2	2	1	1	1	1	1	1
SiO_2	60.07	58.99	58.40	56.25	55.74	61.58	55.20	55.24	54.90	54.44	54.27	53.97	53.66	52.68	53.80	53.58	53.32
	(0.18)	(0.31)	(0.71)	(0.48)	(0.32)	(1.51)	(0.35)	(0.58)	(0.24)	(0.37)	(0.25)	(0.25)	(0.31)	(0.22)	(0.32)	(0.33)	(0.40)
TiO_2	0.84	0.85	0.87	0.96	1.07	0.76	1.08	1.03	1.02	0.95	0.93	0.88	0.87	0.85	0.90	0.90	0.90
	(0.08)	(0.08)	(0.07)	(0.11)	(0.06)	(0.03)	(0.07)	(0.04)	(0.04)	(0.05)	(0.10)	(0.04)	(0.04)	(0.04)	(0.06)	(0.06)	(0.04)
Al_2O_3	17.31	17.21	17.93	17.94	17.90	17.30	17.74	17.77	17.63	17.72	17.75	17.69	17.91	17.75	17.11	17.72	18.44
	(0.10)	(0.11)	(0.08)	(0.06)	(0.11)	(0.21)	(0.17)	(0.13)	(0.13)	(0.17)	(0.23)	(0.13)	(0.13)	(0.14)	(0.20)	(0.23)	(0.24)
FeO[T]	5.97	6.30	5.98	7.00	7.13	5.30	6.89	6.72	7.15	7.23	7.41	7.19	7.15	7.26	7.49	7.41	7.33
	(0.13)	(0.10)	(0.45)	(0.14)	(0.18)	(0.66)	(0.18)	(0.31)	(0.12)	(0.22)	(0.12)	(0.12)	(0.28)	(0.10)	(0.15)	(0.11)	(0.05)
MnO	0.08	0.09	0.08	0.11	0.16	0.10	0.13	0.11	0.12	0.13	0.12	0.12	0.14	0.13	0.14	0.12	0.13
	(0.05)	(0.09)	(0.04)	(0.05)	(0.05)	(0.03)	(0.02)	(0.02)	(0.02)	(0.03)	(0.01)	(0.02)	(0.02)	(0.03)	(0.02)	(0.01)	(0.02)
MgO	3.55	3.79	3.76	4.82	5.32	3.38	4.65	4.64	5.14	5.23	5.66	6.20	6.41	7.51	8.08	6.76	6.80
	(0.03)	(0.05)	(0.15)	(0.09)	(0.08)	(0.26)	(0.06)	(0.15)	(0.04)	(0.08)	(0.07)	(0.03)	(0.08)	(0.05)	(0.14)	(0.04)	(0.04)
CaO	6.25	6.35	6.56	7.02	7.03	5.95	7.03	6.82	6.82	7.12	7.12	7.21	7.43	7.73	7.61	7.94	7.97
	(0.20)	(0.22)	(0.23)	(0.18)	(0.15)	(0.38)	(0.13)	(0.16)	(0.23)	(0.15)	(0.25)	(0.20)	(0.14)	(0.22)	(0.20)	(0.15)	(0.14)
Na_2O	3.91	4.02	3.93	3.96	4.04	3.91	3.95	4.06	3.97	3.93	3.93	3.77	3.75	3.65	3.69	3.87	3.63
	(0.09)	(0.09)	(0.18)	(0.11)	(0.21)	(0.09)	(0.08)	(0.11)	(0.06)	(0.07)	(0.08)	(0.07)	(0.07)	(0.06)	(0.06)	(0.04)	(0.12)
K_2O	1.61	1.53	1.38	1.12	1.11	1.70	1.23	1.19	1.18	1.12	1.07	0.86	0.77	0.76	0.81	0.85	0.78
	(0.02)	(0.02)	(0.05)	(0.03)	(0.03)	(0.11)	(0.02)	(0.11)	(0.02)	(0.03)	(0.02)	(0.01)	(0.07)	(0.01)	(0.09)	(0.04)	(0.01)
P_2O_5	0.26	0.26	0.24	0.23	0.29	0.20	0.35	0.25	0.34	0.29	0.30	0.26	0.25	0.21	0.17	0.24	0.20
	(0.01)	(0.01)	(0.03)	(0.04)	(0.01)	(0.09)	(0.02)	(0.09)	(0.02)	(0.03)	(0.03)	(0.04)	(0.05)	(0.05)	(0.03)	(0.02)	(0.02)
Total	99.85	99.39	99.13	99.41	99.79	100.18	98.25	97.83	98.27	98.16	98.56	98.15	98.34	98.53	99.80	99.39	99.50
	(0.22)	(0.41)	(0.77)	(0.25)	(0.32)	(0.54)	(0.39)	(0.39)	(0.44)	(0.30)	(0.53)	(0.23)	(0.38)	(0.24)	(0.35)	(0.39)	(0.54)

Values in parentheses are 1 standard deviation uncertainties based on 10 analyzed points for each glass.

contain brick-red lithic fragments. At Site B, to the north, the tan tephra lies directly on the oxidized soil.

The basal sequence is everywhere overlain by an ash bed, which is overlain by a widespread and thick (25 cm at site C) lapilli bed that contains both black and tan clasts but no red lithic fragments. All deposits are stratified, with alternating coarse and fine layers (Fig. 5B). Ash layers typically become thicker and finer towards the top of the stratigraphic sequence (Fig. 5C), reflecting the waning activity at the crater (Pioli et al., 2008). Late-stage bombs litter proximal areas in the western quadrant of the volcano.

Correlation of individual tephra layers throughout the entire deposit was not possible, although some layers could always be traced between adjacent pits. One distinctive tan tephra bed appears in most of the sites to the east of the volcano, approximately halfway through the stratigraphy (Fig. 5D). It seems likely that this bed records the opening of the Sapichu vent, which lay to the east of the main vent and produced ash that was characterized as "very spongy" (Foshag and González-Reyna, 1956). Restriction of distinctive (easily correlated) beds to limited sectors of the volcano is consistent with the low eruption column height of individual explosions, which would have been easily influenced by local winds. The near-circularity of the bulk isopach map is the integrated product of several years of intermittent activity under different seasonal wind patterns (Pioli et al., 2008).

4.2. Textural observations

The tan tephra, black scoria and dense clasts are all moderately to highly crystalline (Fig. 6). The most obvious difference between the three components is their average vesicularity, which Pioli et al. (2008) determined from density measurements to be 64%, 55%, and <20%, respectively. BSE images also show that black clasts have a more crystalline groundmass than the tan clasts, with abundant tiny late-stage oxides (Fig. 6C), and that dense clasts are holocrystalline. Because both black and dense clasts are found as inclusions within tan tephra (Fig. 6D), but tan clasts do not occur as inclusions within the black or dense clasts, we have interpreted the denser (and more crystalline) clasts to have been modified by degassing and crystallization within the cone itself (Pioli et al., 2008).

Tan clasts from the lowest lapilli beds in sections B and C are distinctive in having large (300–400 μm) plagioclase crystals (Fig. 6A,B). Plagioclase phenocrysts have also been described in the earliest lava sample (Feb. 22, 1943) and in the earliest bombs (Luhr, 2001). All other basaltic andesite lavas lack phenocrysts of plagioclase, with the exception of lava erupted immediately after the Sapichu period (Wilcox, 1954). Olivine occurs as both phenocrysts and microlites; olivine phenocrysts often show spectacular skeletal growth morphologies and plagioclase concentrations around their margins (Fig. 6E,F).

Tan clasts from the middle to upper parts of the tephra sequence are remarkable in their textural uniformity (Fig. 6G,H). Plagioclase microphenocryst and microlite abundance is 35–40%, accompanied by 5–7% mafic phases (olivine and clinopyroxene). Plagioclase crystals are elongated in cross-section (tabular in 3D), and often aligned. Pyroxene crystals are typically small (10–20 μm) and euhedral, whereas olivine microlites are often rounded with hopper morphologies (Fig 6G). Scattered olivine phenocrysts are commonly skeletal, with growth features that are similar to those observed in the basal tephra (Fig. 6F). Inclusions of less vesicular and more crystalline clasts (typically 1–3 mm in size) are common in the tan tephra clasts (Fig. 6D); the cryptocrystalline to holocrystalline groundmass of these inclusions (Fig. 6I) shows them to be included fragments of black scoria and dense lava. Some denser clasts have vesicle textures that record compaction-related deformation (Fig. 6J). Clasts from the uppermost part of Site A (Phase 3) have pyroxene reaction rims on olivine (Fig. 6K). A late-stage breadcrust bomb has the same groundmass crystal assemblage but is unusual in having a population of tiny plagioclase microlites in addition to microphenocrysts (Fig. 6L).

Please cite this article as: Erlund, E.J., et al., Compositional evolution of magma from Parícutin Volcano, Mexico: The tephra record, Journal of Volcanology and Geothermal Research (2009), doi:10.1016/j.jvolgeores.2009.09.015

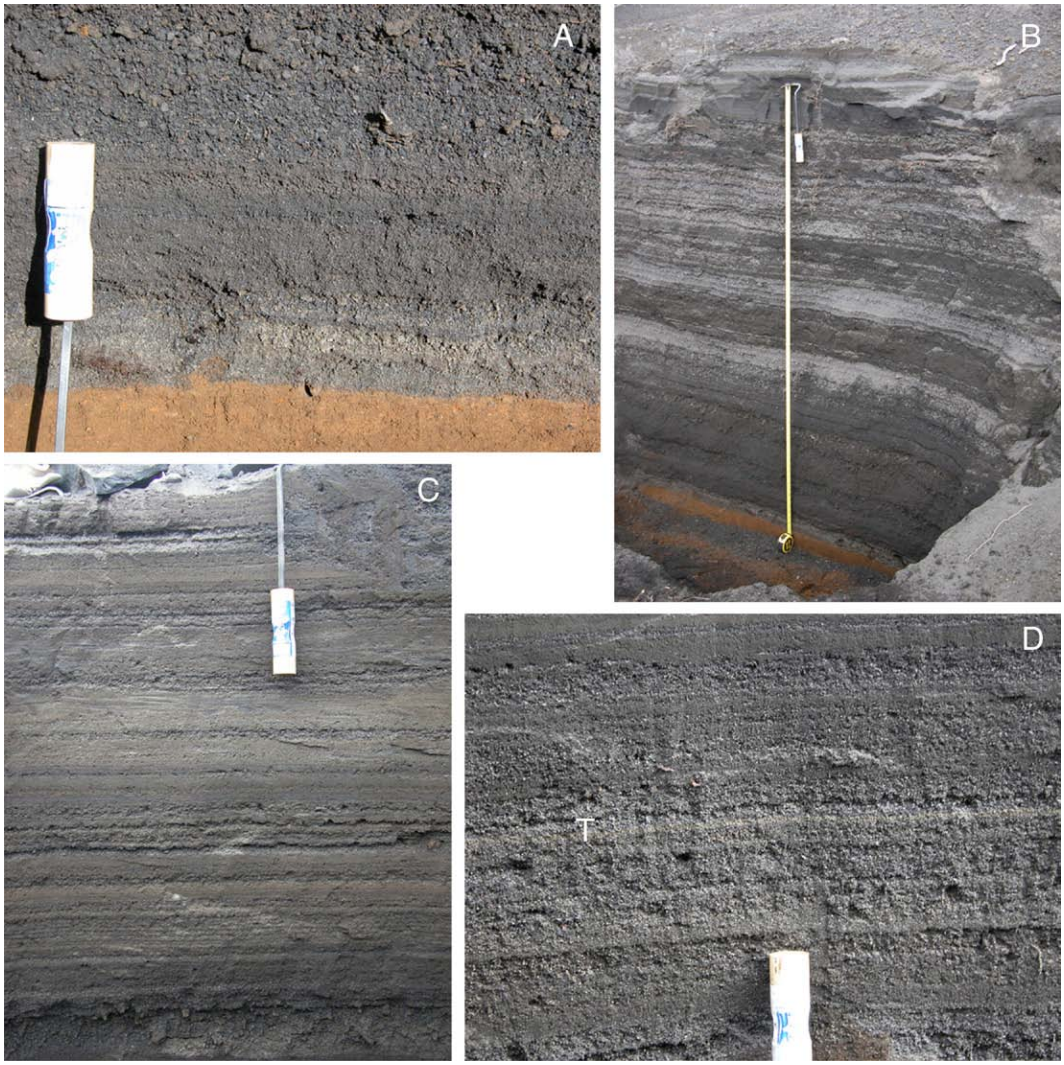

Fig. 5. Outcrop photos. (A) Basal section exposed 2.5 km south of the vent (labeled [155] on Fig. 4); note pronounced light colored layer and upper thick lapilli sequence. (B) Entire preserved section from (A) illustrating the characteristic alternating layers of ash and lapilli. (C) Uppermost ash-dominated tephra sequence at Site C. (D) Thin golden pumice layer (labeled T) preserved in the eastern sector of the volcano (labeled 50 on Fig. 4) that we tentatively correlate with the Sapichu episode.

Early erupted tan clasts are distinctive in having a well developed population of plagioclase microlites in addition to a well developed plagioclase phenocryst population (Fig. 6A,B). The difference between this microlite population and the microphenocryst population that characterizes the main phase of violent Strombolian activity (Fig. 6G, H) can be quantified by measurement of crystal size distributions (CSDs; Fig. 7). CSDs from the main phase of activity show linear CSDs to ~0.5 mm, with average number densities of ~10^6/mm^3. The microlite population of the early tephra, in contrast, shows an increase in plagioclase crystals with an average size <100 μm; distinct curvature in the CSD the requires multiple nucleation events. Crystal number densities of the microlite population are more than an order of magnitude higher than those of the microphenocrysts, indicating nucleation under conditions of high undercooling that were most likely triggered by rapid decompression and degassing of volatile-rich early melts (e.g. Pioli et al., 2008).

4.3. Compositional data

4.3.1. Bulk compositions

The bulk compositions that we have obtained for juvenile tephra samples are compared to bulk tephra analyses in Luhr (2001), lava analyses in Wilcox (1954), early bombs from Foshag and González-Reyna (1956), and melt inclusion analyses (Luhr, 2001) in Fig. 8. Our data, which span from the earliest to the latest erupted magma, range from 52.7 to 61.6 wt.% SiO_2, bracketing the compositional range of the lavas (55–60 wt.% SiO_2; Wilcox, 1954) and dated tephra (54.7–58.5 wt.% SiO_2; Luhr, 2001). Similarly, MgO varies from 3.4 to 8.1 wt.% compared with 3.5–5.8 wt.% in the lavas (Wilcox, 1954) and 4.4–5.8 wt.% in the dated tephra (Luhr, 2001). This compositional overlap indicates not only that the tephra sections span the same compositional range as the lavas, but that they also provide new compositional information about both the earliest (most primitive) and latest (most evolved) stages of the eruption.

The compositional evolution of the earliest stages of the Parícutin eruption is not well-documented in the literature. Wilcox (1954) analyzed only two lava samples from the energetic Quitzocho period (Feb–Oct, 1943), one from February 22 and one from March of 1943. Luhr (2001) analyzed two additional tephra samples, one from May 26 and one from August 1, 1943. Foshag and Gonzalez-Reyna (1956) report analyses from two early bombs that were collected by local farmers during the first few days of the eruption. Because these bombs have compositions that are considerably less evolved than the earliest Wilcox sample they have long been considered suspect. However, the bulk composition of tan tephra from basal tephra layers exposed in sections C and D encompasses the composition of one of these bombs

Please cite this article as: Erlund, E.J., et al., Compositional evolution of magma from Parícutin Volcano, Mexico: The tephra record, Journal of Volcanology and Geothermal Research (2009), doi:10.1016/j.jvolgeores.2009.09.015

(Fig. 8), lending credence to the argument that at least one of these samples represents very early juvenile Parícutin magma (Luhr and Housh, 1993; Luhr, 2001).

The late-stage evolution of Parícutin's magma is captured by bulk tephra analyses from the upper section A and late-stage bombs. The tephra samples have andesitic compositions (58.4–60.1 wt.% SiO_2, 3.6–3.8 wt.% MgO and 1.4–1.6 wt.% K_2O) that correspond to analyses reported by Wilcox (1954) for lava erupted after mid-1947. The bomb sample is more evolved, with 61.6% SiO_2, 3.3% MgO and 1.7% K_2O. In general, these analyses follow trends expected to result from assimilation of silicic material (Wilcox, 1954; McBirney et al., 1987), although a single trend does not encompass all of the variation observed in these samples. In particular, we see more variation in MgO at about 55 wt.% SiO_2 than seen in the lava samples (Fig. 8C). This is not surprising given the strong olivine control exhibited by the more primitive compositions.

Pioli et al. (2008) used the bulk data to place the tephra stratigraphy within a temporal framework. We summarize that correlation in Fig. 9 by creating a normalized stratigraphic section, which allows us to constrain Luhr's Phase 1–Phase 2 boundary to normalized stratigraphic heights between 0.28 and 0.49 within section C, or about 1/3 of the way up our composite stratigraphy. These bounds are consistent with estimates by Fries (1953) that about 46% of the tephra volume was erupted in 1943, and the eyewitness accounts of the most energetic activity (and heaviest ash fall) occurring between late March and early June (that is, during Phase 1).

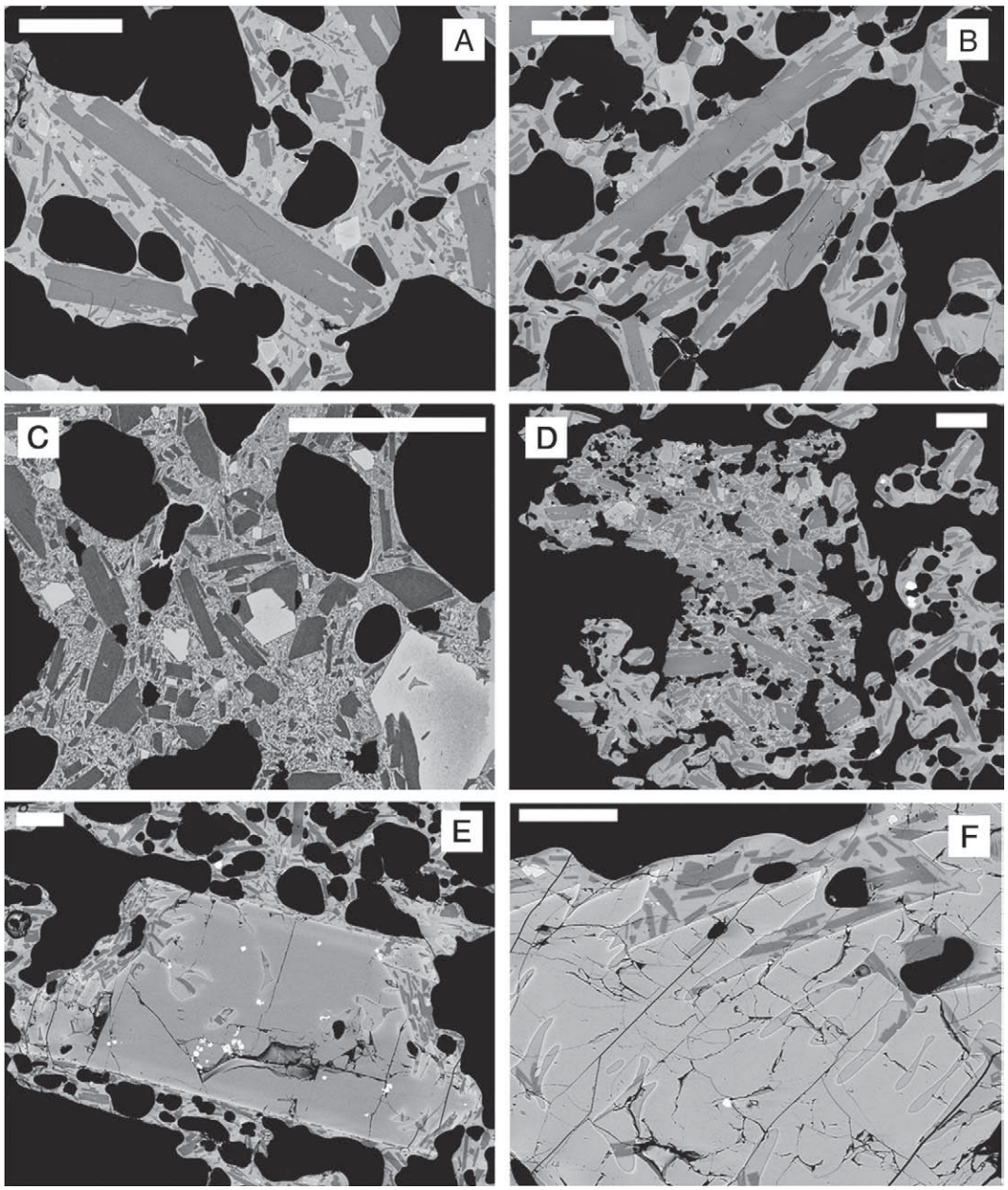

Fig. 6. BSE images of Parícutin tephra. Scale bar is 100 μm unless otherwise indicated. (A) Basal tan tephra from Site B (PADA12f) showing the plagioclase phenocrysts and numerous tiny microlites. (B) Tan tephra from the lowest thick lapilli layer at Site C (P-2007-8c) showing identical features to the basal tephra from Site B. (C) Basal black scoria from Site B (PADA12f) showing the high groundmass crystallinity, particularly of Fe–Ti oxides. (D) Black scoria inclusion within tan tephra in lowest thick lapilli layer at Site C (P-2007-8c). (E) Skeletal olivine crystal in tan tephra (P-2007-8c). (F) Close-up of skeletal olivine from Phase 2 (PAR4_6c). (G) Phase 2 tan tephra (PAR4_6c). (H) Upper Phase 2 tephra (PARZ2c). (I) Dense inclusion within Phase 2 tan tephra (PAR4_6c) showing cryptocrystalline groundmass; scale bar is 20 μm. (J) Black scoria clast from Phase 2 showing deformed vesicles (PADA9i). (K) Closeup of groundmass in upper Phase 2 tephra (PADA3a) showing reaction rim of pyroxene surrounding olivine crystals; scale bar is 25 μm. (L) Groundmass in the quenched rind of a late-stage bomb; note zoning on plagioclase microphenocrysts and numerous late-stage microlites; note 10 μm scale bar in the lower righthand corner.

Please cite this article as: Erlund, E.J., et al., Compositional evolution of magma from Parícutin Volcano, Mexico: The tephra record, Journal of Volcanology and Geothermal Research (2009), doi:10.1016/j.jvolgeores.2009.09.015

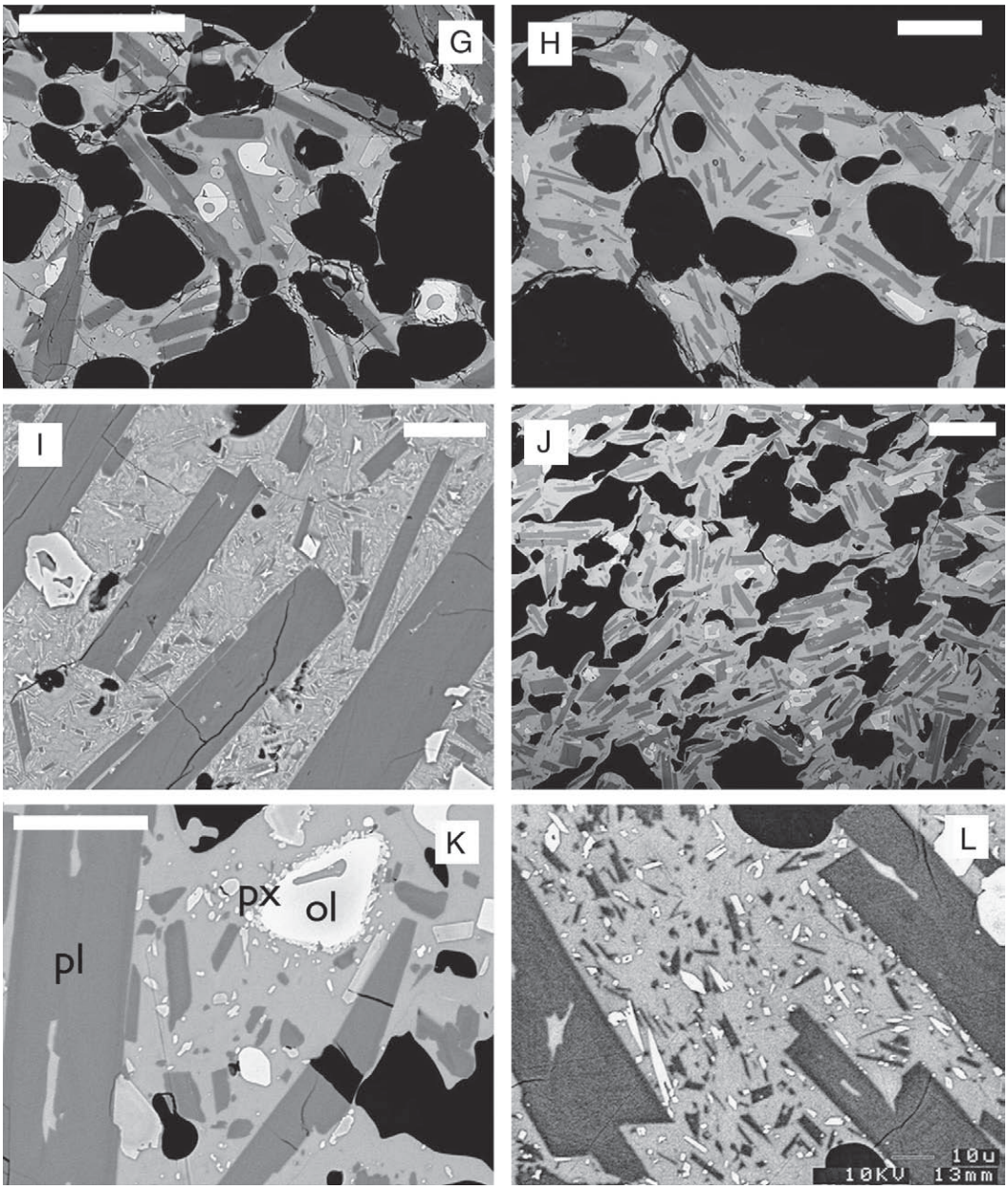

Fig. 6 *(continued).*

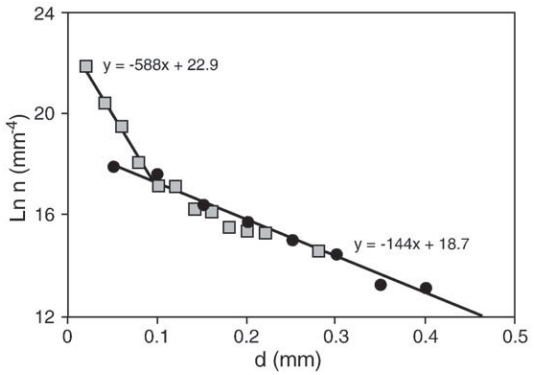

Fig. 7. Comparison of groundmass plagioclase CSDs from two samples: basal tan tephra (PADA12f, squares) and Phase 2 tan tephra (PAR4_6c, circles). Samples have overlapping microphenocryst populations but the basal tephra contains a microlite population that is missing from the Phase 2 tephra.

4.3.2. Glass compositions

A striking feature of Fig. 8 is the deviation of many melt inclusion compositions from bulk tephra trends, which indicates that they have trapped evolved, rather than primitive, melts. Matrix glass compositions (Fig. 10) provide a more detailed look at late-stage melt evolution. As noted previously by Luhr (2001), there are some elements (illustrated by K_2O) for which matrix glasses conform to, and extend, the trends shown for the bulk compositions. Other elements (illustrated by Al_2O_3 and TiO_2) deviate from the bulk compositional trends. For example, both matrix glass and melt inclusion analyses show increasing TiO_2 with increasing SiO_2, while matrix glass analyses for Phase 3 tephra are not colinear with either the Phase 1–2 trend or the andesite bulk compositions, which have decreasing TiO_2 with increasing SiO_2. These deviations of matrix glass compositions from the array of bulk compositions provide evidence that processes other than simple crystallization differentiation created the variations in bulk compositions. The ramifications of this for distinguishing

Please cite this article as: Erlund, E.J., et al., Compositional evolution of magma from Parícutin Volcano, Mexico: The tephra record, Journal of Volcanology and Geothermal Research (2009), doi:10.1016/j.jvolgeores.2009.09.015

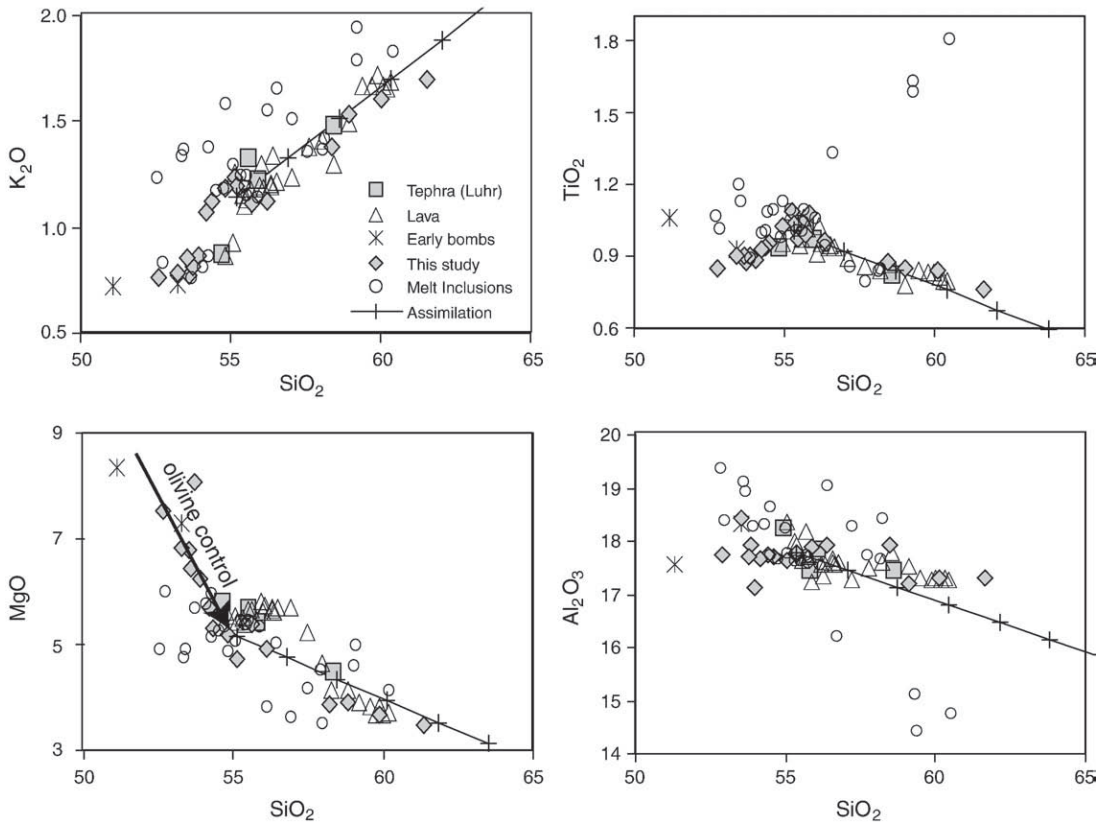

Fig. 8. Harker diagrams showing compositional variations for bulk tephra (this study and Luhr, 2001), lava (Wilcox, 1954), early bombs (Foshag and González-Reyna, 1956), and olivine-hosted melt inclusions (Luhr, 2001). Symbols as shown in the legend. The line shows magma compositions formed by mixing of the average xenolith composition (McBirney et al., 1987) and the average of Phase 2 bulk tephra. Tick marks show 10% intervals. Arrow in C shows the effect of 7 wt.% equilibrium olivine fractionation.

effects of assimilation and fractional crystallization are discussed below (Section 5.3).

4.3.3. Olivine compositions

An independent measure of tephra composition is provided by analysis of loose olivine phenocrysts collected throughout the tephra sequence (Pioli et al., 2008). Most of these olivine crystals are broken, probably reflecting rupturing of overpressured melt inclusions, and some are skeletal (Fig. 6E,F). Core compositions of the largest olivines are generally homogeneous, although many crystals are normally zoned with Fe-rich rims.

Olivine core compositions decrease in forsterite (Fo) content with increasing stratigraphic height (Table A3). Olivine cores from basal layers at Sites B, C and D are more Mg-rich ($Fo_{86.2}$) than any previously

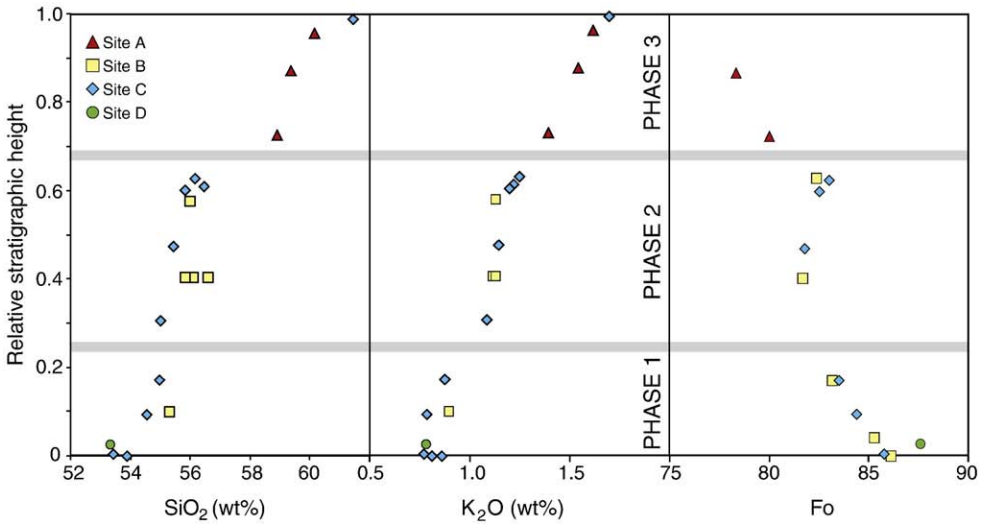

Fig. 9. Variations of bulk tephra and olivine compositions with relative stratigraphic height for the four sites studied. Sites were correlated using both compositional criteria and eyewitness accounts of the eruption, as described in text. To construct a representative tephra section we normalized the stratigraphic heights of section B (total thickness = 5.25 m) to the total thickness of section C (6.35 m); we retain different symbols so that the locations can be distinguished. Site A (post-1946) is above section C. Because of variations in total thickness between Sites A and C (Fig. 4), the lower (pre-1947) part of our composite section is effectively thinner by half than it would actually have been at the proximal locality of Site A.

Please cite this article as: Erlund, E.J., et al., Compositional evolution of magma from Parícutin Volcano, Mexico: The tephra record, Journal of Volcanology and Geothermal Research (2009), doi:10.1016/j.jvolgeores.2009.09.015

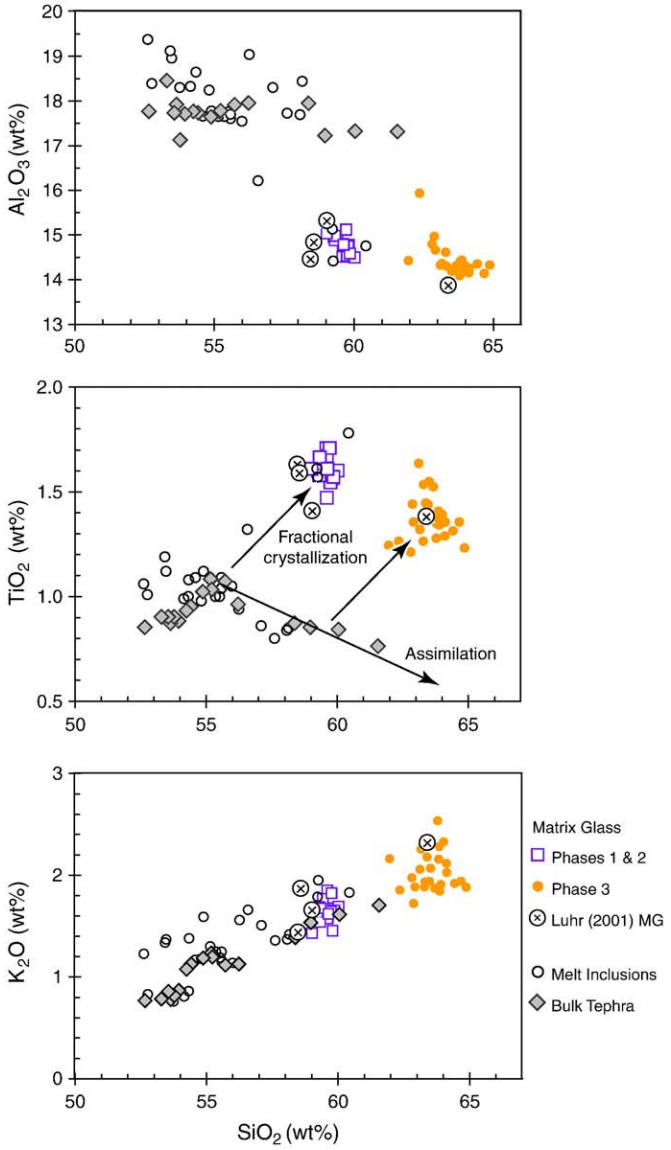

Fig. 10. Harker diagrams showing a comparison of bulk tephra and lava with matrix glass from tephra. Arrows show effects of fractional crystallization and assimilation of average xenoliths.

analyzed ($Fo_{80.2–84.2}$; Bannister et al., 1998; Luhr, 2001). These early samples also show the greatest Fo variability between phenocrysts in the same sample ($Fo_{83.9}$ to $Fo_{88.4}$). Olivine cores from Phase 3 tephra have more Fe-rich compositions ($Fo_{78.3}$) than any previously analyzed. Olivine data support correlations shown in Fig. 9, which indicate that the basal sequence is correlative with Luhr's Phase 1, that tephra sections B and C contain tephra from Phases 1 and 2 but not Phase 3 (except late-stage bombs), and that section A comprises only andesitic (Phase 3) tephra.

To test whether the olivine phenocrysts were in equilibrium with the melts in which they erupted, we calculated Fe–Mg exchange distribution coefficients (K_d) using the method of Toplis (2005), which includes the effects of temperature (from Luhr, 2001), pressure (from melt inclusion volatile contents), melt composition and dissolved H_2O content. Because increases in SiO_2 and H_2O content both cause an increase in K_d, the calculated K_d value for Paricutin melts (0.34 ± 0.02) is higher than the value of 0.30 that is typical for basaltic melts. The results of the K_d calculations demonstrate that in many tephra samples, the olivine cores were in equilibrium with their host melts (Fig. 11). However, a few tephra samples have olivine core

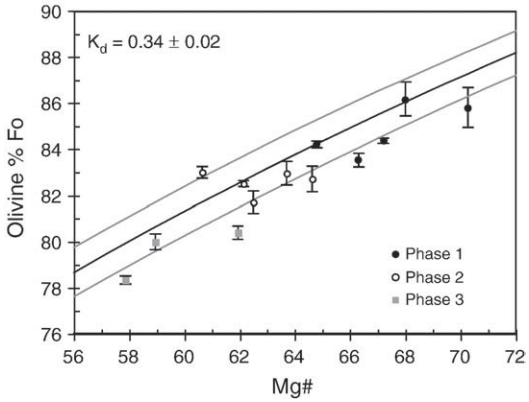

Fig. 11. Olivine core composition vs. bulk tephra Mg#. Olivine and bulk tephra data are from this study (Tables 1, 3 and Appendix Table 3) and from Luhr (2001). Mg# was calculated assuming bulk tephra $FeO/FeO^T = 0.78$ after Luhr (2001). The solid and gray curves are calculated equilibrium values between olivine and melt using $K_d = 0.34 \pm 0.02$ calculated from Toplis (2005) using bulk tephra compositions. Error bars show ± 1 standard deviation in the olivine compositions for each sample.

compositions that are too Fe-rich to have been in equilibrium with their host melts. This could be the result of entrainment of earlier formed crystals by subsequent batches of magma rising through the system (e.g., Johnson et al., 2008) or other magma mixing processes. The normal zoning of most olivine crystals is consistent with the lower Mg/Fe ratios of the matrix glasses caused by relatively late-stage crystallization of olivine ± clinopyroxene ± orthopyroxene.

5. Discussion

The close observed correlation between tephra and lava compositions, mineral assemblages, and textures supports physical models that have a common source for these two eruptive products throughout the eruption (e.g., Krauskopf, 1948; Pioli et al., 2008) and points to the importance of considering both lava and tephra in dynamical studies of violent Strombolian activity. More importantly, our ability to place the tephra deposits within a temporal framework allows us to use the wealth of observational data for this eruption to examine relationships between physical conditions of eruption and compositional changes in the erupted magma. This integration of geochemical and volcanological data allows us to infer temporal changes in magmatic processes and the configuration of the underlying conduit system.

5.1. Magma compositional evolution and evidence for magma batches

Paricutin stands as a classic example of the compositional effects of crustal assimilation. We follow Luhr (2001) in using relations between K_2O and TiO_2 to separate effects of assimilation and fractional crystallization in the eruptive products. The upper crustal granitic assimilant has high K_2O and relatively low TiO_2 (McBirney et al., 1987; Luhr, 2001), whereas fractional crystallization increases the concentrations of both elements because titanomagnetite is not in the crystallizing assemblage (Eggler, 1972; McBirney et al., 1987). Phase 1 (February to July 1943) lava, bulk tephra, and melt inclusions all have $K_2O < 1$ wt.% and TiO_2 from 0.85 to 1.01 wt.%. In comparison to the limited compositional range for Phase 1, Phase 2 lava, tephra, and melt inclusions have systematically higher K_2O contents and a greater range of, and positive correlation between, K_2O and TiO_2 (Fig. 12). The covariation of these elements matches predictions for fractional crystallization. Luhr (2001) demonstrates that the apparent small compositional gap between the Phase 1 and 2 compositions (Fig. 12) cannot be explained by fractional crystallization or crustal assimilation or a combination of the two processes. Our data support the existence of this compositional gap, and therefore Luhr's conclusion

Please cite this article as: Erlund, E.J., et al., Compositional evolution of magma from Parícutin Volcano, Mexico: The tephra record, Journal of Volcanology and Geothermal Research (2009), doi:10.1016/j.jvolgeores.2009.09.015

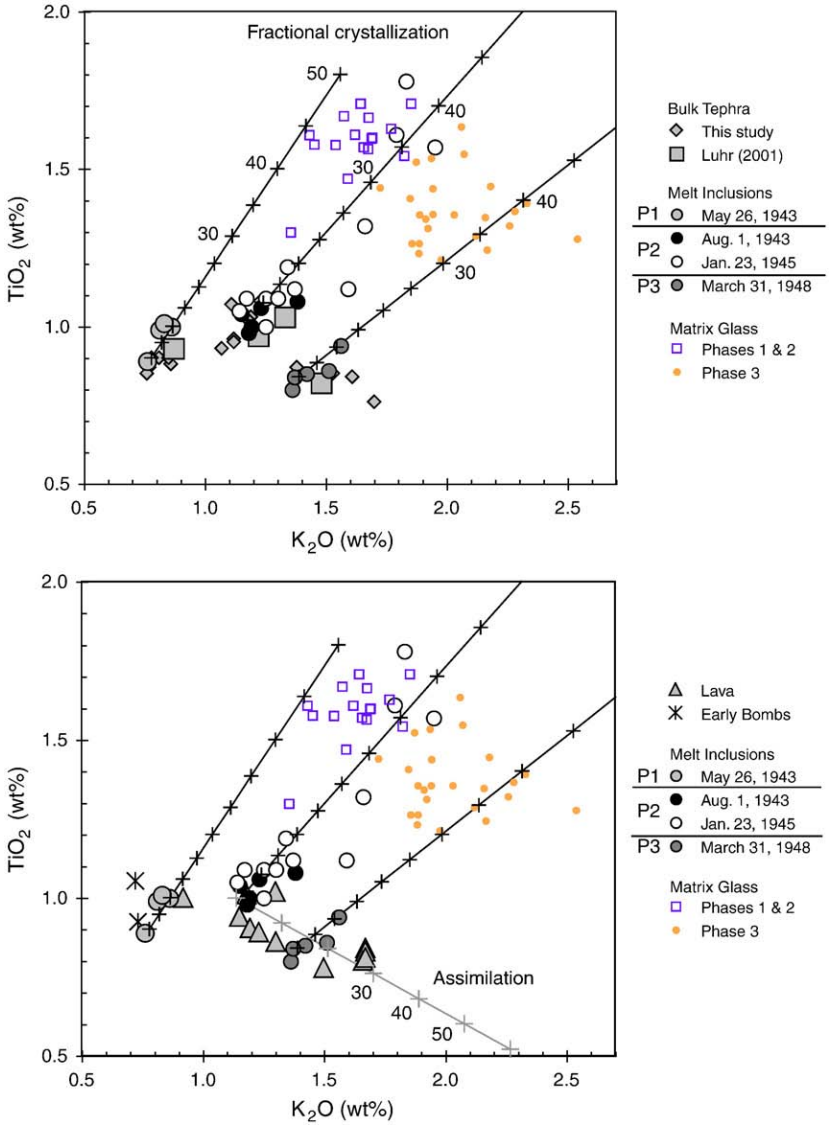

Fig. 12. TiO_2 vs. K_2O for bulk tephra, lava, early bombs, olivine-hosted melt inclusions, and matrix glass. Data sources as in Fig. 9. Fractionation lines emanating from Phase 1, 2, and 3 bulk compositions are calculated assuming perfectly incompatible behavior of TiO_2 and K_2O and are marked in 5% increments. Mixing line (light gray) for assimilation is calculated as described in Fig. 9.

that Phases 1 and 2 involved two compositionally distinct magma batches.

The onset of Phase 3 in mid-1947 is defined by the abrupt compositional evolution of lavas from basaltic andesite to andesite (Fig. 3), interpreted to reflect assimilation of granitic country rock (Wilcox, 1954; McBirney et al., 1987). Over time, lava compositions had progressively higher K_2O and lower TiO_2 as a result of the low TiO_2 of the crustal assimilant (Fig. 12). Melt inclusions and bulk tephra erupted after 1946 share these characteristics, although our data also show a compositional gap in the tephra between Phase 2 and Phase 3. We interpret this gap to reflect a change in eruption style that preceded the compositional change, as indicated by both a decrease in grain size observed in later Phase 2 deposits at site C and the absence of Phase 3 tephra at medial to distal locations (Pioli et al., 2008).

Bulk tephra samples and quenched matrix glasses are related along lines of constant TiO_2/K_2O because of in situ crystallization of microphenocrysts and microlites (Fig. 12). Matrix glass compositions therefore provide information about whether individual pyroclasts are related to Phase 1, 2 or 3 magma. Matrix glass compositions from most early tephra samples have TiO_2/K_2O ratios that are similar to either Phase 1 or 2 lavas, bulk tephra, and melt inclusions, and show an overall increase in matrix glass K_2O and K_2O/TiO_2 with increasing stratigraphic height (Fig. 13) that is consistent with the temporal change in the lavas and bulk tephra compositions. Matrix glasses from Site A (post-1946) tephra show a range of TiO_2/K_2O ratios that are consistent with in situ crystallization of variably contaminated Phase 3 magmas. They do not show the simple linear change in bulk composition seen in lava and bulk tephra compositions. This appears to be a characteristic of the matrix glasses, which generally exhibit a more continuous range of TiO_2/K_2O values than the bulk tephra samples. This could be caused by either the effects of minor, late-stage crystallization of groundmass titanomagnetite or by mixing of magma from different phases.

5.2. Eruption conditions

Stratigraphic controls (Figs. 9 and 13) allow us to correlate both deposits and tephra characteristics to detailed observations of eruptive activity. Here we combine the physical characteristics of the deposits (Pioli et al., 2008) with textural and compositional information to examine three important phases of the Parícutin eruption: (1) initial conditions of magma ascent, (2) 'cineritic' (violent

Please cite this article as: Erlund, E.J., et al., Compositional evolution of magma from Parícutin Volcano, Mexico: The tephra record, Journal of Volcanology and Geothermal Research (2009), doi:10.1016/j.jvolgeores.2009.09.015

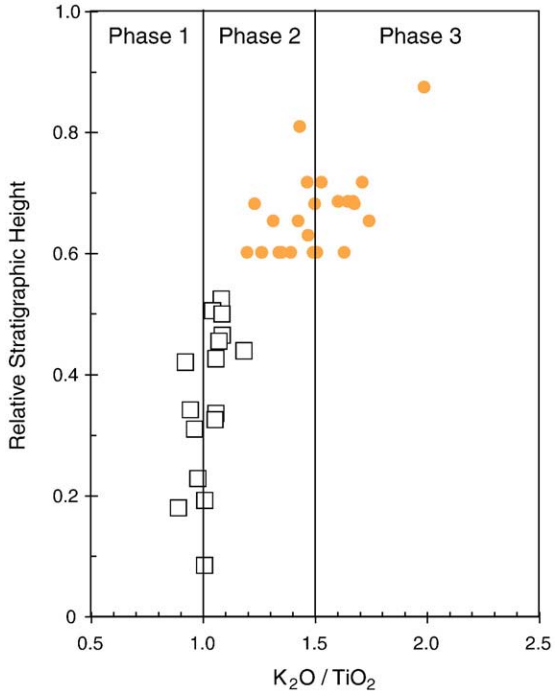

Fig. 13. Changes in matrix glass composition with stratigraphic height as illustrated by variations in the K_2O/TiO_2 ratio, which best discriminates the effects of fractionation from those of assimilation (see text for discussion). Dividing lines between the compositions of Phase 1, 2 and 3 material are based on bulk tephra and lava data in Fig. 13.

Strombolian) activity that produced the bulk of the tephra deposit, and (3) late-stage Strombolian to Vulcanian activity.

5.2.1. Eruption initiation

The basal eruptive sequence forms a distinctive marker bed that is best preserved to the southwest of the vent (Fig. 5A). We interpret the thin dark basal layer to represent deposition from the first eruptive column formed in the evening of Feb 20, 1943. Localization of this layer to the S and SW sectors is consistent with descriptions of the plume being bent toward Tancitaro (to the SW). The more widely distributed vesicular tephra bed above this layer indicates more energetic explosions, probably those of the first few days of activity. Ash beds that cap the basal sequence represent diminished tephra production that accompanied cone growth in late February and early March, 1943.

The bulk composition of the basal tephra is the least evolved of any magma produced during the nine-year eruption. Melt inclusions within the olivine crystals have H_2O contents of 1.3–4.2 wt.%, encompassing the entire range measured by Luhr (2001) and indicating entrapment over pressures of 50 to 400 MPa (Pioli et al., 2008). Most of the melt inclusions also contain CO_2, suggesting deeper crystallization and less degassing than melt inclusions from later in the eruption (e.g., Luhr, 2001). The tephra samples have high plagioclase crystallinities (~35%) and crystal sizes that range from phenocrysts to microlites (Figs. 6 and 7). Phase relations (Moore and Carmichael, 1998; Johnson et al., 2008) indicate that crystallization of plagioclase and pyroxene was driven by degassing rather than cooling. Together these observations suggest that magma ascended from depth sufficiently quickly to prevent substantial fractionation by olivine settling but at the same time was arrested temporarily at sufficiently shallow levels (<~100 MPa based on phase diagram of Moore and Carmichael, 1998) to allow limited plagioclase phenocryst growth, perhaps during the >45 days of unrest that preceded the eruption (e.g., Yokoyama and de la Cruz-Reyna, 1990). The only other plagioclase-phyric samples erupted during the first year of activity were from resumption of activity at the main vents, immediately following the 2.5 months of activity at the Sapichu vent.

5.2.2. Quitzocho episode (February–October, 1943)

This episode was dominated by the 'heavy cineritic' phase of activity that began on March 18 and produced the heaviest tephra fall of the eruption. Our stratigraphic constraints suggest that >1/3 of the tephra at Site C was deposited during this time period (consistent with observations of Fries, 1953). Energetic activity at the vent then resumed in late July. It is probably not a coincidence that the break in activity between early June and late July corresponds to the time interval that separates eruption of Phase 1 and Phase 2 magma batches (Luhr, 2001). In fact, it seems likely that resumption of vigorous eruptive activity in late July signalled the arrival of the Phase 2 magma batch at the surface.

In contrast to the variability of the earliest erupted material, tan tephra produced during Phase 2 is distinctive in its homogeneity in bulk composition, matrix glass composition, olivine composition, and groundmass textures. Important attributes of Phase 2 tan tephra include a remarkably constant bulk composition coupled with a constant but considerably more evolved groundmass glass composition that requires ~30–40% of syn-ascent, degassing-driven crystallization, similar to values documented for Jorullo (Johnson et al., 2008). This homogeneity suggests that the magma delivery system (that is, the dikes and sills that connected the deep magma source to the vent) was well established and relatively stable during this time period.

A comparison of melt inclusion and matrix glass compositions provides further insight into the evolution of the subvolcanic magma storage system during this time period. Melt inclusions in the earliest erupted Phase 2 magma (the August 1, 1943, tephra sample of Luhr, 2001) have compositions that are similar to the bulk composition and retain some CO_2. In contrast, melt inclusions from a later Phase 2 (1945) tephra sample have no CO_2, and are more evolved than the bulk composition, with some that overlap with measured groundmass glass compositions (Fig. 12). These most evolved melt inclusions require as much as 40% fractional crystallization from the bulk. That such evolved compositions were trapped as inclusions in olivine indicates that by January 1945, a shallow body of degassed magma resided in a dike and/or sill-like magma body beneath the cone. Similar evidence for shallow magma storage and crystallization has been found in other cinder cone eruptions (Cervantes and Wallace, 2003a; Johnson et al., 2008, this volume). It is possible that establishment of this subvolcanic magma storage complex contributed to the decrease in average eruption rate from 1943 to 1946 (Fig. 2). Longer magma residence at shallow levels would also have permitted extensive pre-eruptive degassing (confirmed by the prevalence of melt inclusion trapping pressures <100 MPa) responsible for the increasing importance of effusive activity over this time period.

5.2.3. Phase 3—the waning phase

The change in eruptive style from the violent Strombolian eruptions of Phases 1 and 2 (Foshag and González-Reyna, 1956) to a dominance of lava effusion later in the eruption was associated with a decrease in the average mass eruption rate (Fig. 2). Although this change in eruptive style was roughly coincident with the compositional shift from basaltic andesite to andesite, the increasing thickness and abundance of ash layers at the top of stratigraphic section C (Fig. 5C) shows that the explosive activity diminished at the end of Phase 2, before the compositional shift that marked Phase 3 (Fig. 10). Thus it appears that the declining mass eruption rate was responsible for shifting the balance of the eruption from explosive to effusive (e.g., Pioli et al., 2009) and that the compositional change followed.

Phase 3 activity also included Vulcanian explosions caused by alternating pressurization and disruption of a 'rock plug' located at the

Please cite this article as: Erlund, E.J., et al., Compositional evolution of magma from Parícutin Volcano, Mexico: The tephra record, Journal of Volcanology and Geothermal Research (2009), doi:10.1016/j.jvolgeores.2009.09.015

bottom of the vent (e.g., Wilcox, 1947). The observed increasing strength, but decreasing frequency, of the explosions through time suggests that the strength of the lava plug increased with longer repose intervals. Our textural data show evidence for both compaction/densification of shallow magma (Fig. 6J) and late-stage groundmass crystallization (Fig. 6L) that provide evidence for extensive degassing of the uppermost magma within the conduit during the latest phase of the eruption.

5.3. Implications for the magma plumbing system and depths of assimilation

The volatile content of melt inclusions records the pressure of crystallization, which places minimum constraints on the depth of magma residence just prior to eruption. Olivine-hosted melt inclusions from Parícutin were trapped at maximum pressures of ~400 MPa (Luhr, 2001; Johnson et al., this volume). Assuming an upper crustal density of 2600 kg/m^3, this suggests maximum olivine crystallization depths of ~14 km during the early part of the eruption (Phase 1). These depths are similar to those estimated for early melts at nearby Jorullo volcano (Johnson et al., 2008).

Melt inclusion data for Phase 2 and 3 magmas are limited to a few data points from Luhr (2001). Although these data are sparse, they indicate a pulse of rapid olivine crystallization (based on olivine and melt inclusion morphologies) in Phase 2 and 3 melts at <100 MPa (<3.8 km depth). The relatively low pressures of crystallization (mostly ≤100 MPa) indicated by Phase 2 and 3 melt inclusions at Parícutin indicate temporary storage and crystallization of melts within a shallow dike and sill complex. The wide range of pressures (~50 to 400 MPa) shown by Phase 1 melt inclusions, combined with the textural evidence for temporary magma arrest, further suggest that this shallow storage complex started to form during the initial stages of magma ascent. Evidence for shallow crystallization of olivine accompanying the eruption of other young monogenetic scoria cones in Mexico (Cervantes and Wallace, 2003b; Johnson et al., 2008, this volume) suggests that syn-eruptive development of shallow magma storage regions is a common feature of MGVP monogenetic eruptions.

Capture of rising magma by faults has been demonstrated theoretically (Gaffney et al., 2007) as well as in the field (Valentine and Krogh, 2006), and seems likely in regions of extension, such as the MGVF. If the 45 days of precursory seismic activity recorded at Parícutin (Yokoyama and de la Cruz-Reyna, 1990) records the time period of initial development of a shallow storage system, we can infer the amount of magma that may have been stored in the upper crust prior to the onset of eruption. Assuming a magma supply rate equivalent to the average mass eruption rate for Phase 1 (8×10^4 kg/s; Pioli et al., 2008), we calculate that ~0.1 km^3 of magma could have accumulated in a dike and sill complex prior to the onset of eruptive activity (less that 10% of the total erupted volume of 1.3 km^3; Fries, 1953).

A shallow dike and sill network beneath the volcano would have promoted crustal assimilation by creating a relatively large surface area in contact with the granite wallrock (e.g., Dungan, 2005). Edwards and Russell (1998) have used computational simulations to predict timescales of weeks to years for assimilation-fractional crystallization processes in mafic magmas, although assimilation can be more rapid when the assimilant has been pre-heated. Observers noted that eruption of partially melted granitic xenoliths was common during the Sapichu period of the Paricutin eruption, when activity migrated to a dike-fed subsidiary vent about 7 months into the eruption (e.g., Krauskopf, 1948). This provides evidence of sufficient heating for partial melting of granite basement within the first year of the eruption.

Compositional data for bulk tephra, melt inclusions, and matrix glass from Phases 1 and 2 do not show chemical evidence of assimilation. However, the scatter in TiO_2/K_2O ratios for matrix glass and a few Phase 2 melt inclusions (Fig. 13) could reflect small amounts of shallow contamination. In contrast, Phase 3 lavas, bulk tephra, melt inclusions and matrix glass all show clear evidence for assimilation, demonstrating that by 1947 there was widespread melting of wallrocks and xenolithic blocks in the shallow subvolcanic magma system.

These data suggest an alternative model to a pre-existing large zoned magma chamber as the source of all of Parícutin's eruptive products (e.g., Wilcox, 1954; McBirney et al., 1987). If such a zoned magma chamber had existed, we would expect at least some of the melt inclusions from the early parts of the eruption to show the chemical effects of granite contamination because most crystallization would occur in strongly contaminated thermal boundary layers. Instead, it seems more likely that assimilation occurred during the eruption, as magma was intruded into shallow sills below the growing cinder cone (e.g., Dungan, 2005). While eruption rates were high, deep magma fed both the eruption and sill formation (Fig. 14A). As mass eruption rate decreased because of diminished magma supply from depth (Scandone, 1979), the more stagnant, contaminated magma residing in the peripheries of the dike and sill complex started to feed the eruption, eventually becoming the dominant erupting component (Fig. 14B). The apparent linear change in bulk composition coupled with the range in the K_2O/TiO_2 content of the matrix glass throughout Phase 3 suggests that the withdrawal process was reasonably, but not perfectly, efficient in mixing the various magma compositions.

The volume of magma erupted between early 1947 (the onset of compositional change) and the end of the eruption was ~0.3–0.4 km^3 (Fries, 1953), or 3–4 times our estimate of pre-eruption contributions to the dike and sill complex. This ratio seems reasonable, given the expectation that early phases of the eruption would have continued to feed sill formation, and that extraction of magma from those sills would not be perfectly efficient.

6. Conclusions

The data presented above show that tephra deposits preserve a wealth of information about the compositional and textural evolution of magma during cinder cone eruptions and provide a record that is

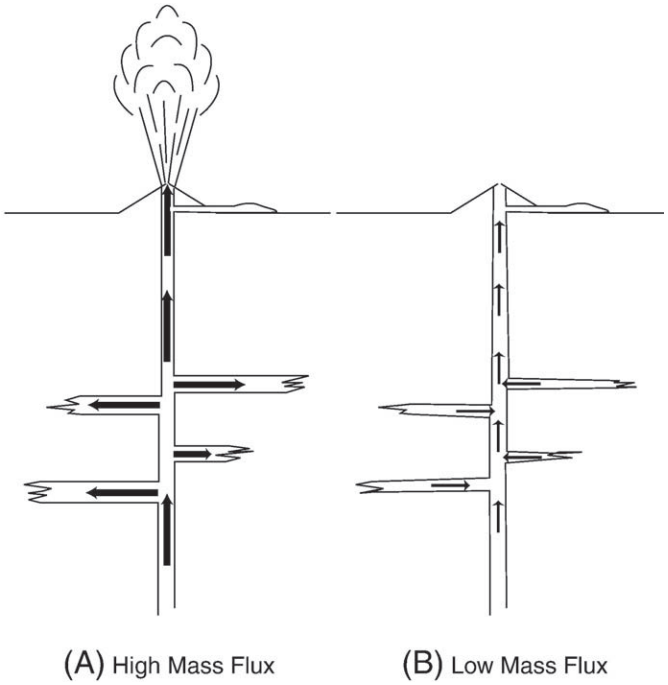

Fig. 14. Cartoon of the magma feeder system beneath Parícutin volcano to illustrate both filling (A) and tapping (B) of the subsurface magma storage system under different mass eruption rates.

Please cite this article as: Erlund, E.J., et al., Compositional evolution of magma from Parícutin Volcano, Mexico: The tephra record, Journal of Volcanology and Geothermal Research (2009), doi:10.1016/j.jvolgeores.2009.09.015

complementary to the lava record that has been preferred, traditionally, for petrologic studies. The tephra analyses presented here show a greater compositional range of material than previous studies, particularly in primitive basal samples. At the same time, combined petrologic analysis of tephra and lava samples can provide insight into magma storage and ascent conditions that are often overlooked by physical volcanology studies of tephra deposits.

Tephra sections are placed in a temporal framework by correlating compositional and textural characteristics with tephra samples of known eruption date (Luhr, 2001) and with the lava record (Wilcox, 1954). We confirm Luhr's (2001) classification of the early erupted material (Feb–July 1943; Phase 1) as compositionally distinct from magma erupted during the bulk of the explosive activity (Aug 1943 through 1946; Phase 2). We also show that the arrival of the Phase 2 magma batch in August, 1943 was associated with renewed vigor of explosive activity. An abrupt decrease in grain size toward the end of Phase 2 (Pioli et al., 2008) shows that the eruption intensity decreased prior to the shift in magma composition to andesite, which marked the onset of Phase 3 in 1947. These time constraints demonstrate that magma supply rate, not composition, was the primary control on eruptive behavior (e.g., Pioli et al., 2009).

Finally, we provide evidence for the early development of a shallow magma storage system (probably in the form of a dike and sill complex) and suggest that magma residing within this storage region was the source of evolved Phase 3 magma. Relatively low pressures of crystallization (equivalent to depths ≤4 km) inferred from melt inclusion data for Phase 2 and Phase 3 are consistent with formation of a shallow dike and sill complex that would have promoted crustal assimilation by creating a relatively large surface area in contact with the granite wallrock. Melt inclusion and matrix glass data demonstrate that degassing of H_2O-rich (≤4.2 wt.%) magmas as they ascended into this shallow reservoir resulted in extensive crystallization; this would have released additional latent heat (e.g., Blundy et al., 2006) that would have aided assimilation. We further hypothesize that this evolved magma was withdrawn from shallow storage regions in response to diminished rates of magma supply from depth. In this way, the dynamics of magma ascent through primary conduit systems may control the extent to which magma is stored within, or tapped from, intermediate storage levels.

Acknowledgements

We would first like to recognize the inspiration and support for this work that Jim Luhr provided—we miss him a lot. We also gratefully acknowledge an insightful review by Greg Valentine, particularly for suggesting that the precursory activity may reflect initial formation of shallow sills. We also thank Robert Trumbull for his careful editorial comments, Anne Peslier for acting as Associate Editor, and Joop Varenkamp, for assembling this tribute volume in Jim Luhr's memory. This work was funded by NSF EAR0510493 to KC and PW and EAR0309559 to PW.

Appendix

Appendix Table 1
Sample list showing type of compositional analysis performed. MG = matrix glass analysis.

Sample	Site	Strat. height	Material analyzed	Analysis method
PADA-Up_A	A	2.60	MG: Tan	microprobe
			MG: Black	microprobe
			MG: Dense	microprobe
PADA-Up_B	A	2.39	Bulk: Tan	EPMA on glass bead
PADA-Up_E	A	1.76	MG: Tan	microprobe
			MG: Black	microprobe
			MG: Dense	microprobe
PADA-Up_G	A	1.64	MG: Tan	microprobe
			MG: Black	microprobe
PADA-Up_H	A	1.52	olivine	microprobe
PADA-Up_I	A	1.48	Bulk: Tan	EPMA on glass bead
PADA-Up_L	A	1.18	MG: Tan	microprobe
PADA-Up_N	A	0.87	MG: Tan	microprobe
			MG: Black	microprobe
PADA-Up_O	A	0.82	MG: Tan	microprobe
PADA-Up_P	A	0.55	MG: Tan	microprobe
			MG: Black	microprobe
PADA-Up_Q	A	0.40	olivine	microprobe
			Bulk: Tan	EPMA on glass bead
			MG: Dense	microprobe
PADA-Up_S	A	0.02	MG: Tan	microprobe
			MG: Black	microprobe
PADA-Lo_2a	B	5.25	olivine	microprobe
PADA-Lo_2b	B	5.05	MG: Tan	microprobe
			MG: Black	microprobe
PADA-Lo_3a2	B	4.96	MG: Tan	microprobe
			MG: Black	microprobe
PADA-Lo_3b	B	4.79	Bulk: Tan	XRF
			MG: Black	microprobe
PADA-Lo_4b	B	4.55	MG: Tan	microprobe
			MG: Black	microprobe
			MG: Dense	microprobe
PADA-Lo_5a	B	4.39	MG: Tan	microprobe
			MG: Black	microprobe
PADA-Lo_5b	B	4.34	MG: Tan	microprobe
			MG: Black	microprobe
PADA-Lo_5d	B	4.20	MG: Black	microprobe
			MG: Dense	microprobe
PADA-Lo_6c	B	3.42	MG: Tan	microprobe
PADA-Lo_6d	B	3.36	olivine	microprobe
			Bulk: Tan	XRF & EPMA on glass bead
			MG: Black	microprobe
			MG: Dense	microprobe
PADA-Lo_7a	B	3.26	MG: Tan	microprobe
			MG: Black	microprobe
			MG: Dense	microprobe
PADA-Lo_7b	B	3.11	MG: Tan	microprobe
			MG: Black	microprobe
			MG: Dense	microprobe
PADA-Lo_9d	B	2.29	MG: Black	microprobe
PADA-Lo_9i	B	2.17	MG: Tan	microprobe
PADA-Lo_10a	B	1.93	MG: Black	microprobe
PADA-Lo_10b	B	1.80	MG: Tan	microprobe
PADA-Lo_11c	B	1.44	olivine	microprobe
PADA-Lo_11h	B	1.03	MG: Tan	microprobe
			MG: Black	microprobe
PADA-Lo_11j	B	0.85	Bulk: Tan	XRF
			MG: Tan	microprobe
			MG: Black	microprobe
PADA-Lo_12d	B	0.37	olivine	microprobe
PADA-Lo_12f	B	0.01	olivine	microprobe
			MG: Tan	microprobe
			MG: Black	microprobe
Bomb	C	6.35	bomb	EPMA on glass bead
P-2007_11	C	6.31	olivine	microprobe
			Bulk: Tan	EPMA on glass bead
P-2007_17	C	6.14	Bulk: Tan	EPMA on glass bead
P-2007_19a	C	6.04	olivine	microprobe
			Bulk: Tan	EPMA on glass bead
P-4-06_2c1	C	4.76	Bulk: Tan	EPMA on glass bead
P-4-06_4c	C	3.10	Bulk: Tan	EPMA on glass bead
P-2007_3a	C	1.75	olivine	microprobe
			Bulk: Tan	EPMA on glass bead
P-2007_6a	C	0.97	olivine	microprobe
			Bulk: Tan	EPMA on glass bead
P-2007_9b	C	0.08	olivine	microprobe
			Bulk: Tan	EPMA on glass bead
P-2007_10	C	0.03	Bulk: Dense	EPMA on glass bead
P-5-06_3	D	–	Bulk: Tan	EPMA on glass bead
P-5-06_1	D	–	olivine	microprobe

Please cite this article as: Erlund, E.J., et al., Compositional evolution of magma from Parícutin Volcano, Mexico: The tephra record, Journal of Volcanology and Geothermal Research (2009), doi:10.1016/j.jvolgeores.2009.09.015

Appendix Table 2
Electron microprobe analyses of matrix glasses.

Sample number	Grain number	Component	*n*	SiO_2	1σ	TiO_2	1σ	Al_2O_3	1σ	FeO	1σ	MnO	1σ	MgO	1σ	CaO	1σ	Na_2O	1σ	K_2O	1σ	P_2O_5	1σ	Total	1σ
PADA-Up_L	1	tan	6	63.71	(0.24)	1.34	(0.14)	13.94	(0.20)	7.33	(0.15)	0.16	(0.06)	2.13	(0.25)	4.13	(0.18)	3.38	(0.57)	1.91	(0.05)	0.38	(0.04)	98.39	(0.57)
PADA-Up_L	2	tan	6	63.71	(0.63)	1.30	(0.21)	14.20	(0.33)	7.21	(0.12)	0.14	(0.06)	2.10	(0.14)	4.36	(0.21)	3.51	(0.53)	1.90	(0.10)	0.37	(0.02)	98.79	(0.75)
PADA-Up_L	3	tan	6	63.93	(0.70)	1.22	(0.14)	14.12	(0.14)	7.40	(0.11)	0.16	(0.06)	2.13	(0.05)	4.18	(0.26)	3.07	(0.94)	1.85	(0.06)	0.38	(0.03)	98.44	(0.61)
	Mean			63.78	(0.12)	1.28	(0.06)	14.08	(0.13)	7.31	(0.10)	0.15	(0.01)	2.12	(0.02)	4.22	(0.12)	3.32	(0.22)	1.89	(0.03)	0.38	(0.00)	98.54	(0.22)
PADA-Up_N	1	tan	6	63.11	(0.25)	1.32	(0.18)	14.35	(0.21)	7.57	(0.10)	0.13	(0.05)	2.21	(0.10)	4.24	(0.29)	4.21	(0.46)	2.25	(0.50)	0.43	(0.04)	99.81	(0.34)
PADA-Up_N	2	tan	6	63.27	(0.27)	1.34	(0.14)	14.29	(0.15)	7.25	(0.12)	0.10	(0.08)	2.11	(0.08)	4.25	(0.25)	3.86	(0.50)	2.14	(0.03)	0.44	(0.03)	99.04	(0.42)
PADA-Up_N	3	tan	6	63.33	(0.29)	1.36	(0.18)	14.14	(0.18)	7.51	(0.18)	0.08	(0.06)	2.09	(0.05)	4.13	(0.11)	3.78	(0.40)	2.26	(0.07)	0.44	(0.02)	99.11	(0.38)
	Mean			63.23	(0.11)	1.34	(0.02)	14.26	(0.11)	7.44	(0.17)	0.10	(0.03)	2.14	(0.07)	4.21	(0.07)	3.95	(0.23)	2.22	(0.07)	0.43	(0.01)	99.32	(0.43)
PADA-Up_N	1	black	6	63.00	(0.33)	1.27	(0.20)	14.82	(0.51)	7.12	(0.17)	0.09	(0.06)	2.12	(0.13)	4.48	(0.31)	3.93	(0.42)	1.89	(0.12)	0.37	(0.03)	99.08	(0.54)
PADA-Up_N	2	black	6	63.08	(0.35)	1.30	(0.12)	14.07	(0.19)	7.64	(0.24)	0.15	(0.07)	2.10	(0.10)	4.39	(0.21)	3.83	(0.37)	2.12	(0.10)	0.40	(0.03)	99.07	(0.64)
PADA-Up_N	3	black	6	62.87	(0.45)	1.42	(0.12)	14.53	(0.48)	7.26	(0.38)	0.10	(0.04)	2.08	(0.17)	4.46	(0.22)	4.31	(0.49)	1.82	(0.54)	0.36	(0.03)	99.21	(0.62)
	Mean			62.98	(0.10)	1.33	(0.08)	14.47	(0.38)	7.34	(0.27)	0.11	(0.03)	2.10	(0.02)	4.44	(0.05)	4.02	(0.25)	1.94	(0.16)	0.38	(0.02)	99.12	(0.08)
PADA-Up_O	1	tan	6	63.40	(0.37)	1.27	(0.20)	14.00	(0.24)	7.31	(0.20)	0.14	(0.06)	2.06	(0.05)	4.36	(0.13)	3.63	(0.57)	2.09	(0.06)	0.44	(0.03)	98.71	(0.49)
PADA-Up_O	2	tan	6	63.61	(0.53)	1.38	(0.21)	14.21	(0.21)	7.33	(0.30)	0.15	(0.07)	2.01	(0.11)	4.09	(0.24)	3.76	(0.38)	2.31	(0.18)	0.44	(0.02)	99.29	(0.45)
PADA-Up_O	3	tan	6	63.44	(0.37)	1.34	(0.15)	14.11	(0.12)	7.50	(0.15)	0.10	(0.06)	2.17	(0.19)	4.19	(0.19)	3.52	(0.57)	2.01	(0.07)	0.45	(0.05)	98.83	(0.53)
	Mean			63.48	(0.11)	1.33	(0.05)	14.11	(0.11)	7.38	(0.11)	0.13	(0.03)	2.08	(0.08)	4.21	(0.14)	3.64	(0.12)	2.14	(0.16)	0.44	(0.00)	98.94	(0.30)
PADA-Up_P	1	tan	6	63.23	(0.20)	1.51	(0.10)	14.22	(0.19)	7.63	(0.22)	0.13	(0.05)	2.23	(0.06)	4.36	(0.18)	3.69	(0.51)	1.86	(0.03)	0.35	(0.03)	99.21	(0.56)
PADA-Up_P	2	tan	6	63.29	(0.40)	1.39	(0.15)	14.31	(0.21)	7.52	(0.22)	0.09	(0.04)	2.14	(0.06)	4.37	(0.22)	3.69	(0.51)	1.83	(0.06)	0.35	(0.02)	98.98	(0.51)
PADA-Up_P	3	tan	6	63.14	(0.35)	1.33	(0.20)	14.01	(0.23)	7.68	(0.18)	0.14	(0.05)	2.16	(0.05)	4.34	(0.23)	3.64	(0.46)	1.89	(0.07)	0.36	(0.03)	98.68	(0.62)
	Mean			63.22	(0.08)	1.41	(0.09)	14.18	(0.15)	7.61	(0.08)	0.12	(0.03)	2.18	(0.05)	4.36	(0.02)	3.67	(0.03)	1.86	(0.03)	0.35	(0.01)	98.96	(0.27)
PADA-Up_S	1	tan	6	62.15	(1.33)	1.26	(0.38)	15.90	(2.65)	6.95	(1.24)	0.13	(0.05)	2.20	(0.45)	5.07	(1.21)	3.68	(0.72)	1.85	(0.40)	0.38	(0.09)	99.57	(0.65)
PADA-Up_S	2	tan	6	63.16	(0.33)	1.54	(0.18)	14.12	(0.26)	7.82	(0.18)	0.14	(0.08)	2.09	(0.04)	4.40	(0.18)	3.57	(0.49)	2.06	(0.04)	0.43	(0.03)	99.33	(0.38)
PADA-Up_S	3	tan	6	62.72	(0.23)	1.63	(0.20)	14.24	(0.18)	7.60	(0.16)	0.15	(0.05)	2.24	(0.07)	4.45	(0.28)	3.76	(0.56)	2.05	(0.08)	0.42	(0.02)	99.26	(0.66)
PADA-Up_S	4	tan	6	63.08	(0.46)	1.44	(0.09)	13.91	(0.21)	7.70	(0.22)	0.11	(0.04)	2.08	(0.12)	4.31	(0.40)	4.18	(0.50)	2.17	(0.43)	0.40	(0.02)	99.38	(0.56)
PADA-Up_S	5	tan	6	62.07	(0.31)	1.42	(0.17)	14.78	(0.16)	7.55	(0.14)	0.12	(0.07)	2.28	(0.08)	4.60	(0.24)	3.73	(0.30)	1.70	(0.05)	0.34	(0.03)	98.60	(0.36)
PADA-Up_S	6	tan	6	62.87	(0.52)	1.43	(0.27)	14.11	(0.11)	7.75	(0.29)	0.12	(0.06)	2.17	(0.08)	4.37	(0.09)	3.81	(0.43)	1.92	(0.11)	0.39	(0.03)	98.92	(0.47)
PADA-Up_S	7	tan	6	62.64	(0.25)	1.35	(0.12)	14.60	(0.21)	7.66	(0.17)	0.16	(0.05)	2.45	(0.09)	4.62	(0.15)	3.69	(0.47)	1.88	(0.05)	0.35	(0.02)	99.40	(0.31)
PADA-Up_S	8	tan	6	62.77	(0.37)	1.25	(0.15)	14.50	(0.40)	7.61	(0.24)	0.11	(0.05)	2.35	(0.11)	4.65	(0.31)	3.59	(0.36)	1.87	(0.06)	0.38	(0.03)	99.08	(0.59)
PADA-Up_S	9	tan	6	62.73	(0.14)	1.52	(0.18)	14.19	(0.13)	7.70	(0.21)	0.10	(0.03)	2.30	(0.03)	4.38	(0.03)	3.76	(0.44)	1.92	(0.05)	0.40	(0.03)	98.99	(0.81)
PADA-Up_S	10	tan	6	62.12	(0.19)	1.20	(0.12)	14.64	(0.18)	7.61	(0.16)	0.08	(0.08)	2.41	(0.07)	4.50	(0.11)	3.91	(0.48)	1.95	(0.05)	0.37	(0.02)	98.78	(0.63)
	Mean			62.63	(0.39)	1.40	(0.14)	14.50	(0.57)	7.59	(0.24)	0.12	(0.02)	2.26	(0.13)	4.53	(0.22)	3.77	(0.17)	1.94	(0.13)	0.39	(0.03)	99.13	(0.31)
PADA-Up_S	1	black	2	64.18	(1.24)	1.84	(0.03)	11.90	(1.49)	7.65	(1.40)	0.07	(0.01)	1.96	(0.57)	3.63	(0.44)	4.23	(1.03)	2.20	(0.79)	0.50	(0.04)	98.14	(1.48)
PADA-Up_S	2	black	6	63.15	(0.44)	1.56	(0.13)	13.67	(0.65)	8.12	(0.32)	0.13	(0.08)	1.84	(0.16)	4.15	(0.49)	4.13	(0.54)	2.06	(0.59)	0.39	(0.03)	99.20	(0.79)
PADA-Up_S	3	black	6	62.63	(0.52)	1.17	(0.10)	14.86	(0.30)	7.16	(0.32)	0.11	(0.05)	2.19	(0.12)	4.61	(0.24)	4.41	(0.17)	1.64	(0.13)	0.33	(0.02)	99.12	(0.41)
PADA-Up_S	4	black	6	63.70	(0.55)	1.39	(0.20)	13.98	(0.33)	7.79	(0.25)	0.11	(0.06)	1.82	(0.03)	4.40	(0.14)	4.03	(0.98)	1.82	(0.09)	0.37	(0.04)	99.44	(0.64)
PADA-Up_S	5	black	6	63.70	(0.42)	1.51	(0.22)	13.71	(0.07)	7.74	(0.26)	0.09	(0.03)	1.76	(0.18)	4.28	(0.40)	4.75	(0.19)	1.58	(0.13)	0.35	(0.02)	99.47	(0.41)
PADA-Up_S	6	black	6	63.43	(0.82)	1.27	(0.15)	14.38	(0.41)	7.09	(0.66)	0.12	(0.10)	2.10	(0.28)	4.08	(0.38)	3.71	(0.48)	2.21	(0.20)	0.33	(0.03)	98.72	(0.58)
	Mean			63.47	(0.53)	1.46	(0.24)	13.75	(1.01)	7.59	(0.39)	0.10	(0.02)	1.95	(0.17)	4.19	(0.34)	4.21	(0.35)	1.92	(0.28)	0.38	(0.06)	99.01	(0.51)

Please cite this article as: Erlund, E.J., et al., Compositional evolution of magma from Parícutin Volcano, Mexico: The tephra record, Journal of Volcanology and Geothermal Research (2009), doi:10.1016/j.jvolgeores.2009.09.015

PADA A	1	black	10	64.61	(0.34)	1.30	(0.09)	13.50	(0.14)	7.12	(0.17)	0.11	(0.02)	1.78	(0.04)	3.99	(0.07)	4.30	(0.13)	2.72	(0.09)	0.46	(0.02)	99.89	(0.41)
PADA A	1	dense	10	64.60	(0.45)	1.30	(0.20)	13.30	(0.71)	7.48	(0.47)	0.14	(0.04)	1.44	(0.20)	3.72	(0.28)	3.90	(0.54)	3.03	(0.20)	0.50	(0.03)	99.41	(0.58)
PADA E	1	tan	10	63.23	(0.30)	1.27	(0.15)	13.97	(0.22)	7.10	(0.10)	0.12	(0.07)	1.94	(0.05)	4.28	(0.09)	4.12	(0.34)	2.52	(0.05)	0.47	(0.03)	99.01	(0.56)
PADA E	1	black	6	63.97	(0.41)	1.52	(0.21)	13.56	(0.15)	7.78	(0.49)	0.11	(0.04)	1.41	(0.14)	3.68	(0.42)	3.94	(0.34)	3.27	(0.74)	0.53	(0.03)	99.77	(0.50)
PADA E	1	dense	10	62.99	(0.52)	1.29	(0.15)	13.93	(0.26)	7.51	(0.61)	0.10	(0.07)	1.62	(0.11)	3.95	(0.37)	3.86	(0.59)	3.01	(0.70)	0.49	(0.04)	98.75	(0.64)
PADA Q	1	tan	10	61.58	(0.19)	1.24	(0.15)	14.34	(0.10)	7.62	(0.15)	0.13	(0.04)	2.49	(0.06)	4.84	(0.08)	4.37	(0.28)	2.15	(0.06)	0.45	(0.03)	99.20	(0.44)
PADA Q	1	dense	9	63.99	(0.73)	1.59	(0.21)	12.93	(0.75)	7.83	(0.52)	0.15	(0.03)	1.17	(0.11)	4.02	(0.59)	3.67	(0.39)	2.87	(0.22)	0.59	(0.03)	99.29	(0.74)
PADA-Lo_2b	1	black	14	59.48	(0.44)	1.50	(0.15)	14.86	(0.26)	8.47	(0.31)	0.16	(0.08)	3.41	(0.10)	5.68	(0.29)	4.23	(0.35)	1.73	(0.09)	0.47	(0.03)	100.00	(0.33)
PADA-Lo_2b	1	tan	14	59.46	(0.29)	1.47	(0.13)	14.67	(0.29)	8.33	(0.22)	0.17	(0.06)	3.40	(0.05)	5.77	(0.22)	4.33	(0.12)	1.59	(0.04)	0.46	(0.04)	99.63	(0.58)
PADA-Lo_2b	1	tan (pajarito)	14	59.21	(0.25)	1.52	(0.13)	14.70	(0.28)	8.27	(0.14)	0.16	(0.05)	3.40	(0.05)	5.66	(0.20)	4.17	(0.13)	1.65	(0.05)	0.46	(0.04)	99.21	(0.42)
PADA-Lo_3a2	1	black	14	59.52	(0.36)	1.62	(0.15)	14.05	(0.26)	8.70	(0.24)	0.16	(0.05)	3.24	(0.09)	5.44	(0.28)	4.41	(0.22)	1.74	(0.08)	0.48	(0.04)	99.36	(0.44)
PADA-Lo_3a2	1	tan (pajarito)	13	59.20	(0.40)	1.63	(0.16)	14.33	(0.17)	8.51	(0.22)	0.18	(0.07)	3.23	(0.11)	5.55	(0.19)	4.32	(0.13)	1.75	(0.09)	0.48	(0.03)	99.18	(0.62)
PADA-Lo_3b	1	black	13	59.70	(0.22)	1.58	(0.14)	14.61	(0.27)	8.54	(0.21)	0.16	(0.08)	3.34	(0.38)	5.29	(0.25)	4.39	(0.15)	1.81	(0.08)	0.50	(0.03)	99.90	(0.36)
PADA-Lo_4b	1	dense	11	59.86	(0.34)	1.66	(0.14)	14.47	(0.21)	8.80	(0.28)	0.14	(0.04)	2.97	(0.18)	5.33	(0.45)	4.49	(0.21)	1.73	(0.52)	0.51	(0.02)	99.97	(0.56)
PADA-Lo_4b	1	black	14	60.07	(0.75)	1.64	(0.15)	14.48	(0.17)	8.46	(0.48)	0.15	(0.08)	3.11	(0.14)	5.15	(0.34)	4.46	(0.25)	1.86	(0.11)	0.51	(0.04)	99.89	(0.34)
PADA-Lo_4b	1	tan (pajarito)	9	58.78	(0.72)	1.57	(0.14)	14.55	(1.22)	8.45	(0.52)	0.20	(0.04)	3.11	(0.23)	5.58	(0.65)	4.26	(0.18)	1.44	(0.15)	0.50	(0.05)	98.44	(1.40)
PADA-Lo_5a	1	black	13	59.82	(0.43)	1.63	(0.11)	14.43	(0.34)	8.59	(0.46)	0.16	(0.04)	3.10	(0.19)	5.36	(0.42)	4.16	(0.70)	1.79	(0.17)	0.49	(0.04)	99.53	(0.62)
PADA-Lo_5a	1	tan	10	59.02	(0.55)	1.54	(0.10)	14.58	(0.33)	7.99	(0.27)	0.13	(0.04)	3.24	(0.16)	5.52	(0.27)	4.35	(0.16)	1.65	(0.06)	0.48	(0.05)	98.51	(0.71)
PADA-Lo_5a	1	tan (pajarito)	11	59.46	(0.14)	1.66	(0.12)	14.23	(0.25)	8.34	(0.18)	0.13	(0.06)	3.15	(0.07)	5.42	(0.14)	4.26	(0.16)	1.61	(0.06)	0.48	(0.03)	98.74	(0.38)
PADA-Lo_5b	1	black	14	60.29	(0.31)	1.59	(0.16)	14.72	(0.22)	8.21	(0.32)	0.16	(0.04)	3.25	(0.17)	5.44	(0.23)	4.57	(0.24)	1.62	(0.16)	0.47	(0.03)	100.34	(0.41)
PADA-Lo_5b	1	tan (pajarito)	12	59.49	(0.41)	1.55	(0.17)	14.64	(0.25)	8.30	(0.22)	0.19	(0.06)	3.36	(0.09)	5.66	(0.15)	4.19	(0.08)	1.62	(0.06)	0.46	(0.03)	99.46	(0.53)
PADA-Lo_5d	1	dense	12	59.66	(0.28)	1.60	(0.16)	14.18	(0.17)	8.83	(0.25)	0.16	(0.03)	3.16	(0.08)	5.32	(0.20)	4.25	(0.16)	1.86	(0.08)	0.49	(0.04)	99.51	(0.39)
PADA-Lo_5d	1	black	13	59.61	(0.34)	1.60	(0.16)	14.68	(0.15)	8.48	(0.42)	0.16	(0.05)	3.15	(0.17)	5.29	(0.42)	4.46	(0.54)	1.83	(0.18)	0.49	(0.04)	99.73	(0.43)
PADA-Lo_6c	1	tan (pajarito)	13	59.56	(0.37)	1.62	(0.12)	14.09	(0.22)	8.56	(0.25)	0.17	(0.08)	3.23	(0.11)	5.48	(0.23)	4.23	(0.16)	1.68	(0.05)	0.49	(0.03)	99.10	(0.38)
PADA-Lo_6d	1	dense	11	59.80	(0.42)	1.71	(0.21)	14.10	(0.25)	9.21	(0.55)	0.17	(0.07)	2.86	(0.15)	5.07	(0.39)	4.03	(0.17)	2.15	(0.05)	0.50	(0.02)	99.59	(0.41)
PADA-Lo_6d	1	black	11	59.60	(0.48)	1.69	(0.14)	14.52	(0.71)	8.49	(0.47)	0.13	(0.05)	2.91	(0.34)	5.41	(0.55)	4.27	(0.30)	1.77	(0.28)	0.50	(0.05)	99.30	(0.49)
PADA-Lo_6d	1	tan	10	59.34	(0.78)	1.66	(0.16)	14.73	(0.87)	8.45	(0.76)	0.16	(0.04)	2.98	(0.23)	5.54	(0.40)	4.46	(0.17)	1.57	(0.13)	0.50	(0.04)	99.39	(0.48)
PADA-Lo_6d	1	tan (pajarito)	12	59.46	(0.45)	1.60	(0.15)	14.69	(0.15)	8.33	(0.24)	0.16	(0.08)	3.29	(0.09)	5.60	(0.13)	4.21	(0.15)	1.53	(0.05)	0.48	(0.03)	99.35	(0.60)
PADA-Lo_7a	1	dense	14	63.17	(0.96)	2.20	(0.28)	12.90	(0.61)	7.80	(0.74)	0.12	(0.04)	1.39	(0.45)	3.45	(0.51)	4.57	(0.48)	2.95	(0.42)	0.89	(0.05)	99.43	(0.44)
PADA-Lo_7a	1	black	12	60.51	(0.37)	1.60	(0.14)	14.52	(0.20)	8.62	(0.55)	0.15	(0.07)	3.05	(0.26)	5.39	(0.27)	4.43	(0.29)	1.53	(0.17)	0.50	(0.04)	100.31	(0.70)
PADA-Lo_7a	1	tan	13	59.92	(0.68)	1.60	(0.16)	14.47	(0.23)	8.33	(0.17)	0.14	(0.05)	3.18	(0.10)	5.41	(0.14)	4.46	(0.21)	1.69	(0.08)	0.50	(0.04)	99.69	(0.92)
PADA-Lo_7b	1	black	13	59.93	(0.35)	1.74	(0.12)	14.41	(0.26)	8.68	(0.34)	0.17	(0.05)	3.20	(0.17)	5.39	(0.13)	4.37	(0.21)	1.74	(0.08)	0.52	(0.03)	100.14	(0.51)
PADA-Lo_7b	1	tan	13	59.53	(0.26)	1.56	(0.12)	14.51	(0.32)	8.39	(0.18)	0.16	(0.07)	3.26	(0.30)	5.34	(0.26)	4.42	(0.18)	1.65	(0.05)	0.49	(0.04)	99.30	(0.45)
PADA-Lo_7b	1	tan (pajarito)	13	59.31	(0.24)	1.59	(0.11)	14.55	(0.15)	8.47	(0.24)	0.14	(0.07)	3.20	(0.05)	5.51	(0.22)	4.19	(0.16)	1.57	(0.05)	0.49	(0.03)	99.03	(0.46)
PADA-Lo_10a	1	black	12	59.14	(0.26)	1.65	(0.21)	14.44	(0.32)	8.44	(0.42)	0.17	(0.05)	3.10	(0.13)	5.24	(0.19)	4.32	(0.39)	1.82	(0.14)	0.51	(0.02)	98.82	(0.66)
PADA-Lo_9d	1	black	2	60.98	(3.53)	0.76	(0.57)	18.09	(5.67)	3.78	(1.58)	0.05	(0.09)	2.05	(0.80)	6.57	(2.64)	4.74	(0.12)	1.66	(0.90)	0.56	(0.25)	99.22	(0.70)
PADA-Lo_10b	1	tan (pajarito)	8	59.36	(0.32)	1.79	(0.14)	14.39	(0.13)	8.91	(0.17)	0.14	(0.03)	3.06	(0.18)	5.41	(0.25)	4.42	(0.12)	1.69	(0.08)	0.52	(0.05)	99.68	(0.33)
PADA-Lo_11h	1	black	12	59.50	(0.36)	1.61	(0.11)	14.27	(0.28)	9.13	(0.45)	0.18	(0.09)	3.33	(0.20)	5.58	(0.39)	4.35	(0.47)	1.64	(0.15)	0.48	(0.03)	100.07	(0.44)
PADA-Lo_11h	1	tan (pajarito)	13	59.40	(0.25)	1.55	(0.13)	14.19	(0.24)	9.04	(0.31)	0.17	(0.05)	3.34	(0.10)	5.68	(0.21)	4.24	(0.22)	1.49	(0.05)	0.47	(0.03)	99.56	(0.37)
PADA-Lo_11j	1	black	11	60.37	(0.64)	1.65	(0.13)	14.39	(0.22)	9.11	(0.49)	0.20	(0.06)	3.24	(0.16)	5.48	(0.22)	4.82	(0.24)	1.24	(0.09)	0.45	(0.03)	100.95	(0.43)
PADA-Lo_11j	1	tan (pajarito)	13	58.94	(0.34)	1.58	(0.11)	14.59	(0.46)	8.84	(0.26)	0.16	(0.05)	3.45	(0.12)	5.77	(0.30)	4.26	(0.21)	1.36	(0.07)	0.45	(0.03)	99.40	(0.39)

Values in parentheses are 1 standard deviation uncertainties based on replicate point analyses.

Please cite this article as: Erlund, E.J., et al., Compositional evolution of magma from Parícutin Volcano, Mexico: The tephra record, Journal of Volcanology and Geothermal Research (2009), doi:10.1016/j.jvolgeores.2009.09.015

Appendix Table 3
Olivine compositions determined by electron microprobe.

Sample	Olivine	*n*	SiO_2	1σ	MgO	1σ	FeO	1σ	NiO	1σ	CaO	1σ	Total	1σ	Fo(%)	1σ
PADA-Up_Q	1	4	38.62	(0.17)	41.45	(0.11)	18.71	(0.11)	0.25	(0.01)	0.12	(0.01)	99.16	(0.28)	79.79	(0.05)
PADA-Up_Q	2	4	38.82	(0.15)	41.56	(0.11)	18.05	(0.29)	0.35	(0.01)	0.11	(0.01)	98.89	(0.44)	80.41	(0.25)
PADA-Up_Q	3	4	38.57	(0.08)	41.22	(0.06)	18.66	(0.20)	0.25	(0.00)	0.13	(0.01)	98.84	(0.25)	79.74	(0.18)
PADA-Up_Q	5	4	38.59	(0.14)	41.59	(0.13)	18.30	(0.36)	0.33	(0.04)	0.12	(0.02)	98.94	(0.41)	80.20	(0.27)
PADA-Up_Q	6	4	38.71	(0.09)	41.31	(0.19)	18.72	(0.26)	0.26	(0.03)	0.13	(0.02)	99.12	(0.44)	79.73	(0.18)
PADA-Up_Q	7	4	38.65	(0.11)	41.60	(0.33)	18.64	(0.50)	0.30	(0.02)	0.12	(0.00)	99.30	(0.62)	79.92	(0.46)
PADA-Up_Q	8	4	38.88	(0.04)	41.89	(0.15)	17.87	(0.17)	0.32	(0.01)	0.11	(0.02)	99.07	(0.01)	80.69	(0.21)
PADA-Up_Q	9	4	38.41	(0.06)	41.53	(0.23)	18.50	(0.34)	0.29	(0.05)	0.12	(0.01)	98.85	(0.21)	80.00	(0.36)
PADA-Up_Q	10	4	38.58	(0.09)	41.40	(0.09)	18.87	(0.28)	0.27	(0.02)	0.12	(0.01)	99.25	(0.26)	79.63	(0.25)
Mean			38.65	(0.14)	41.50	(0.19)	18.48	(0.34)	0.29	(0.04)	0.12	(0.01)	99.05	(0.17)	80.01	(0.35)
PADA-Up_H	1	4	38.46	(0.12)	40.18	(0.58)	20.25	(0.23)	0.26	(0.04)	0.13	(0.01)	99.27	(0.49)	77.96	(0.43)
PADA-Up_H	2	4	38.54	(0.12)	40.37	(0.21)	19.91	(0.43)	0.31	(0.01)	0.11	(0.01)	99.23	(0.28)	78.33	(0.45)
PADA-Up_H	3	4	38.19	(0.22)	40.41	(0.10)	19.77	(0.16)	0.28	(0.01)	0.13	(0.01)	98.78	(0.35)	78.47	(0.16)
PADA-Up_H	5	4	38.73	(0.27)	40.60	(0.12)	19.93	(0.37)	0.27	(0.04)	0.13	(0.01)	99.66	(0.52)	78.41	(0.31)
PADA-Up_H	6	4	38.66	(0.22)	40.51	(0.07)	19.71	(0.19)	0.27	(0.01)	0.12	(0.01)	99.27	(0.36)	78.56	(0.14)
PADA-Up_H	7	4	38.50	(0.11)	40.23	(0.16)	19.86	(0.30)	0.25	(0.01)	0.13	(0.01)	98.98	(0.09)	78.31	(0.31)
PADA-Up_H	8	4	38.45	(0.17)	40.51	(0.06)	19.89	(0.16)	0.27	(0.02)	0.12	(0.00)	99.24	(0.12)	78.41	(0.12)
PADA-Up_H	9	4	38.48	(0.08)	40.36	(0.08)	19.82	(0.17)	0.27	(0.04)	0.12	(0.01)	99.06	(0.28)	78.40	(0.11)
PADA-Up_H	10	4	38.29	(0.11)	40.52	(0.21)	20.14	(0.13)	0.28	(0.02)	0.11	(0.01)	99.35	(0.40)	78.20	(0.10)
Mean			38.48	(0.17)	40.41	(0.14)	19.92	(0.17)	0.27	(0.02)	0.12	(0.01)	99.20	(0.25)	78.34	(0.17)
PADA-Lo_2a	1	4	39.69	(0.14)	42.57	(0.31)	16.47	(0.44)	0.41	(0.04)	0.11	(0.01)	99.25	(0.23)	82.16	(0.47)
PADA-Lo_2a	2	4	39.80	(0.08)	42.98	(0.10)	16.11	(0.23)	0.39	(0.02)	0.11	(0.01)	99.39	(0.37)	82.63	(0.23)
PADA-Lo_2a	3	4	39.66	(0.03)	42.42	(0.15)	16.62	(0.17)	0.33	(0.01)	0.13	(0.02)	99.17	(0.25)	81.98	(0.15)
PADA-Lo_2a	4	4	39.81	(0.04)	42.90	(0.34)	16.20	(0.39)	0.40	(0.03)	0.11	(0.01)	99.43	(0.25)	82.51	(0.44)
PADA-Lo_2a	5	4	39.82	(0.07)	42.91	(0.85)	16.38	(0.71)	0.41	(0.04)	0.12	(0.01)	99.63	(0.39)	82.36	(0.92)
PADA-Lo_2a	6	4	39.97	(0.04)	42.99	(0.11)	16.19	(0.14)	0.39	(0.04)	0.13	(0.01)	99.68	(0.13)	82.56	(0.16)
PADA-Lo_2a	7	4	39.76	(0.06)	43.06	(1.08)	15.93	(1.28)	0.39	(0.03)	0.12	(0.02)	99.25	(0.05)	82.81	(1.45)
PADA-Lo_2a	8	4	39.41	(0.04)	42.11	(0.46)	17.14	(0.54)	0.32	(0.07)	0.12	(0.01)	99.10	(0.23)	81.41	(0.60)
PADA-Lo_2a	9	4	39.71	(0.03)	42.90	(0.20)	16.06	(0.18)	0.40	(0.02)	0.11	(0.01)	99.19	(0.37)	82.64	(0.19)
PADA-Lo_2a	10	4	39.71	(0.02)	43.10	(0.10)	16.13	(0.29)	0.38	(0.04)	0.12	(0.00)	99.44	(0.43)	82.65	(0.24)
Mean			39.74	(0.15)	42.82	(0.33)	16.31	(0.37)	0.38	(0.03)	0.12	(0.01)	99.36	(0.21)	82.40	(0.44)
PADA-Lo_6d	1	4	39.17	(0.11)	42.52	(0.07)	17.17	(0.27)	0.32	(0.02)	0.13	(0.00)	99.31	(0.27)	81.53	(0.21)
PADA-Lo_6d	2	4	39.12	(0.26)	42.17	(0.26)	17.51	(0.65)	0.29	(0.05)	0.13	(0.01)	99.22	(0.33)	81.10	(0.65)
PADA-Lo_6d	3	4	38.76	(0.06)	42.46	(0.16)	17.28	(0.11)	0.37	(0.01)	0.11	(0.02)	98.97	(0.22)	81.41	(0.13)
PADA-Lo_6d	4	4	38.79	(0.08)	42.48	(0.08)	17.67	(0.28)	0.30	(0.01)	0.12	(0.01)	99.36	(0.33)	81.08	(0.23)
PADA-Lo_6d	5	4	38.85	(0.21)	42.91	(0.15)	16.64	(0.39)	0.42	(0.03)	0.12	(0.01)	98.95	(0.26)	82.13	(0.38)
PADA-Lo_6d	6	4	38.90	(0.09)	42.45	(0.14)	17.25	(0.13)	0.32	(0.01)	0.14	(0.01)	99.06	(0.22)	81.43	(0.07)
PADA-Lo_6d	7	4	38.88	(0.04)	43.00	(0.14)	16.68	(0.23)	0.41	(0.02)	0.12	(0.01)	99.08	(0.18)	82.13	(0.25)
PADA-Lo_6d	8	4	38.93	(0.19)	42.52	(0.07)	17.21	(0.03)	0.30	(0.02)	0.13	(0.01)	99.09	(0.13)	81.49	(0.05)
PADA-Lo_6d	9	4	38.99	(0.10)	43.03	(0.12)	16.56	(0.19)	0.40	(0.03)	0.12	(0.01)	99.09	(0.27)	82.24	(0.18)
PADA-Lo_6d	10	4	38.89	(0.12)	43.07	(0.17)	16.37	(0.14)	0.41	(0.01)	0.11	(0.01)	98.86	(0.18)	82.43	(0.15)
Mean			38.90	(0.11)	42.68	(0.33)	17.02	(0.46)	0.36	(0.05)	0.12	(0.01)	99.08	(0.15)	81.72	(0.52)
PADA-Lo_11c	1	4	40.18	(0.21)	44.17	(0.12)	15.96	(0.16)	0.40	(0.02)	0.09	(0.01)	100.80	(0.35)	83.15	(0.14)
PADA-Lo_11c	2	4	39.88	(0.09)	44.15	(0.04)	15.81	(0.14)	0.41	(0.01)	0.14	(0.07)	100.38	(0.23)	83.27	(0.13)
PADA-Lo_11c	3	4	39.70	(0.15)	43.52	(0.43)	16.51	(0.40)	0.32	(0.05)	0.14	(0.01)	100.18	(0.18)	82.45	(0.49)
PADA-Lo_11c	4	4	39.30	(0.22)	44.02	(0.13)	16.06	(0.18)	0.38	(0.01)	0.12	(0.03)	99.88	(0.29)	83.01	(0.19)
PADA-Lo_11c	5	4	39.50	(0.23)	44.28	(0.06)	15.83	(0.11)	0.43	(0.01)	0.12	(0.01)	100.16	(0.36)	83.29	(0.10)
PADA-Lo_11c	6	4	39.57	(0.28)	44.23	(0.15)	15.87	(0.08)	0.40	(0.02)	0.12	(0.03)	100.18	(0.24)	83.25	(0.12)
PADA-Lo_11c	7	4	39.71	(0.11)	44.31	(0.19)	15.85	(0.02)	0.41	(0.03)	0.11	(0.01)	100.38	(0.18)	83.29	(0.06)
PADA-Lo_11c	8	4	39.62	(0.23)	44.23	(0.16)	15.77	(0.12)	0.43	(0.03)	0.11	(0.00)	100.16	(0.29)	83.34	(0.15)
PADA-Lo_11c	9	4	39.64	(0.13)	44.60	(0.20)	15.92	(0.12)	0.36	(0.03)	0.11	(0.02)	100.62	(0.28)	83.32	(0.15)
PADA-Lo_11c	10	4	39.62	(0.16)	44.03	(0.24)	15.97	(0.28)	0.41	(0.02)	0.11	(0.02)	100.15	(0.21)	83.10	(0.31)
Mean			39.62	0.16	44.15	0.29	15.95	0.23	0.39	0.04	0.12	0.01	100.23	0.21	83.15	0.28

PADA-Lo_12d	1	4	40.29	(0.23)	45.84	(0.15)	14.12	(0.05)	0.41	(0.03)	0.10	(0.01)	100.76	(0.37)	85.27	(0.06)
PADA-Lo_12d	2	4	40.04	(0.21)	45.68	(0.18)	14.07	(0.11)	0.39	(0.02)	0.11	(0.04)	100.29	(0.21)	85.27	(0.08)
PADA-Lo_12d	3	4	39.89	(0.36)	45.47	(0.05)	14.23	(0.11)	0.38	(0.01)	0.12	(0.02)	100.09	(0.40)	85.07	(0.10)
PADA-Lo_12d	4	4	40.15	(0.23)	45.28	(0.34)	14.69	(0.48)	0.35	(0.06)	0.12	(0.01)	100.58	(0.19)	84.61	(0.52)
PADA-Lo_12d	5	4	40.28	(0.31)	46.27	(0.85)	13.56	(0.98)	0.39	(0.05)	0.11	(0.02)	100.60	(0.23)	85.88	(1.10)
PADA-Lo_12d	6	4	40.13	(0.18)	45.91	(0.20)	13.92	(0.20)	0.40	(0.04)	0.12	(0.01)	100.49	(0.19)	85.46	(0.23)
PADA-Lo_12d	7	4	39.83	(0.17)	45.52	(0.09)	14.40	(0.02)	0.37	(0.02)	0.12	(0.01)	100.24	(0.27)	84.92	(0.04)
PADA-Lo_12d	8	4	40.20	(0.36)	46.01	(0.05)	14.12	(0.08)	0.39	(0.01)	0.13	(0.02)	100.85	(0.35)	85.31	(0.08)
PADA-Lo_12d	9	4	40.26	(0.21)	46.37	(0.56)	13.18	(0.54)	0.43	(0.03)	0.12	(0.03)	100.36	(0.24)	86.25	(0.64)
PADA-Lo_12d	10	4	39.94	(0.21)	45.46	(0.18)	14.44	(0.36)	0.39	(0.06)	0.10	(0.02)	100.34	(0.13)	84.87	(0.36)
Mean			40.08	0.16	45.77	0.38	14.07	0.47	0.39	0.02	0.12	0.01	100.42	0.23	85.29	0.51
PADA-Lo_12f	1	4	39.93	(0.16)	46.04	(0.31)	13.21	(0.44)	0.41	(0.04)	0.13	(0.01)	99.71	(0.23)	86.14	(0.47)
PADA-Lo_12f	2	4	39.89	(0.26)	45.27	(0.10)	13.70	(0.23)	0.36	(0.02)	0.12	(0.01)	99.33	(0.37)	85.49	(0.23)
PADA-Lo_12f	3	4	39.88	(0.13)	46.05	(0.15)	12.60	(0.17)	0.46	(0.01)	0.13	(0.02)	99.12	(0.25)	86.69	(0.15)
PADA-Lo_12f	4	4	39.83	(0.25)	46.23	(0.34)	12.98	(0.39)	0.40	(0.03)	0.12	(0.01)	99.56	(0.25)	86.39	(0.44)
PADA-Lo_12f	5	4	39.15	(0.18)	42.44	(0.85)	16.67	(0.71)	0.16	(0.04)	0.15	(0.01)	98.57	(0.39)	81.94	(0.92)
PADA-Lo_12f	6	4	39.89	(0.16)	45.28	(0.11)	13.32	(0.14)	0.46	(0.04)	0.13	(0.01)	99.08	(0.13)	85.83	(0.16)
PADA-Lo_12f	7	4	39.83	(0.16)	45.53	(1.08)	13.67	(1.28)	0.41	(0.03)	0.12	(0.02)	99.57	(0.05)	85.58	(1.45)
PADA-Lo_12f	8	4	39.76	(0.12)	45.64	(0.46)	13.32	(0.54)	0.38	(0.07)	0.13	(0.01)	99.23	(0.23)	85.93	(0.60)
PADA-Lo_12f	9	4	39.70	(0.22)	45.88	(0.20)	12.53	(0.18)	0.43	(0.02)	0.12	(0.01)	98.67	(0.37)	86.71	(0.19)
PADA-Lo_12f	10	4	39.80	(0.23)	45.97	(0.10)	12.83	(0.29)	0.44	(0.04)	0.12	(0.00)	99.16	(0.43)	86.46	(0.24)
Mean			39.75	(0.23)	45.37	(1.15)	13.51	(1.26)	0.39	(0.09)	0.13	(0.01)	99.14	(0.35)	85.67	(1.47)
P-5-06_1	1	4	40.35	(0.08)	45.34	(0.08)	13.99	(0.07)	0.29	(0.03)	0.12	(0.02)	100.09	(0.18)	85.25	(0.07)
P-5-06_1	2	4	39.97	(0.12)	43.12	(0.35)	16.96	(0.40)	0.15	(0.04)	0.16	(0.01)	100.37	(0.15)	81.92	(0.47)
P-5-06_1	3	4	40.71	(0.08)	46.43	(0.10)	12.74	(0.15)	0.44	(0.02)	0.11	(0.01)	100.43	(0.09)	86.66	(0.16)
P-5-06_1	4	4	40.64	(0.04)	46.54	(0.07)	12.45	(0.14)	0.43	(0.01)	0.11	(0.01)	100.18	(0.19)	86.95	(0.13)
P-5-06_1	5	4	40.67	(0.06)	46.37	(0.04)	12.70	(0.08)	0.42	(0.03)	0.13	(0.03)	100.29	(0.09)	86.68	(0.08)
P-5-06_1	6	4	40.42	(0.04)	45.10	(0.07)	14.25	(0.12)	0.28	(0.04)	0.11	(0.01)	100.16	(0.10)	84.94	(0.13)
P-5-06_1	7	4	40.58	(0.04)	46.31	(0.16)	12.71	(0.16)	0.42	(0.02)	0.12	(0.02)	100.14	(0.08)	86.66	(0.18)
P-5-06_1	8	4	40.57	(0.10)	45.48	(0.32)	13.45	(0.54)	0.36	(0.05)	0.13	(0.02)	99.99	(0.13)	85.77	(0.58)
P-5-06_1	9	4	40.58	(0.03)	46.22	(0.16)	12.87	(0.06)	0.45	(0.03)	0.10	(0.01)	100.21	(0.18)	86.49	(0.07)
Mean			40.50	(0.23)	45.66	(1.09)	13.57	(1.42)	0.36	(0.10)	0.12	(0.02)	100.21	(0.14)	85.70	(1.58)
P-2007-11	1	4	39.67	(0.04)	44.61	(0.07)	15.24	(0.19)	0.46	(0.01)	0.11	(0.00)	100.09	(0.23)	83.91	(0.17)
P-2007-11	2	4	39.53	(0.04)	43.57	(0.22)	15.95	(0.30)	0.36	(0.04)	0.12	(0.01)	99.54	(0.21)	82.96	(0.32)
P-2007-11	3	4	39.53	(0.09)	43.76	(0.43)	16.15	(0.38)	0.35	(0.05)	0.12	(0.00)	99.91	(0.30)	82.84	(0.45)
P-2007-11	4	4	39.54	(0.05)	43.95	(0.06)	15.68	(0.09)	0.40	(0.01)	0.12	(0.00)	99.70	(0.19)	83.32	(0.07)
P-2007-11	5	4	39.49	(0.05)	43.68	(0.17)	16.38	(0.19)	0.34	(0.03)	0.12	(0.01)	100.02	(0.14)	82.62	(0.21)
P-2007-11	6	4	39.54	(0.10)	43.62	(0.48)	16.23	(0.59)	0.34	(0.06)	0.13	(0.00)	99.85	(0.12)	82.73	(0.68)
P-2007-11	7	4	39.45	(0.06)	44.04	(0.06)	16.36	(0.04)	0.33	(0.01)	0.12	(0.01)	100.30	(0.08)	82.75	(0.04)
P-2007-11	8	4	39.30	(0.09)	43.39	(0.33)	16.47	(0.43)	0.31	(0.05)	0.13	(0.00)	99.60	(0.04)	82.44	(0.49)
P-2007-11	9	4	39.47	(0.07)	43.95	(0.67)	16.03	(0.62)	0.36	(0.06)	0.12	(0.00)	99.93	(0.22)	83.01	(0.76)
P-2007-11	10	4	39.55	(0.09)	44.34	(0.13)	15.76	(0.20)	0.39	(0.02)	0.12	(0.00)	100.16	(0.28)	83.37	(0.17)
Mean			39.07	(0.22)	43.94	(0.51)	15.46	(0.40)	0.38	(0.05)	0.12	(0.01)	99.89	(0.59)	83.51	(0.44)
P-2007-19a	1	4	39.20	(0.07)	43.42	(0.06)	16.62	(0.09)	0.35	(0.02)	0.12	(0.00)	99.72	(0.18)	82.32	(0.06)
P-2007-19a	2	4	39.39	(0.06)	43.64	(0.08)	16.55	(0.06)	0.38	(0.01)	0.13	(0.01)	100.09	(0.07)	82.46	(0.08)
P-2007-19a	3	4	39.43	(0.04)	44.04	(0.13)	16.24	(0.18)	0.37	(0.02)	0.12	(0.00)	100.20	(0.10)	82.86	(0.20)
P-2007-19a	4	4	39.33	(0.05)	43.55	(0.11)	16.25	(0.18)	0.37	(0.05)	0.12	(0.00)	99.62	(0.04)	82.69	(0.19)
P-2007-19a	5	4	39.45	(0.08)	43.75	(0.14)	16.20	(0.22)	0.41	(0.03)	0.12	(0.01)	99.93	(0.16)	82.80	(0.23)
P-2007-19a	6	4	39.26	(0.08)	43.52	(0.11)	16.12	(0.04)	0.40	(0.01)	0.12	(0.01)	99.41	(0.16)	82.79	(0.07)
P-2007-19a	7	4	39.19	(0.02)	43.53	(0.10)	16.46	(0.23)	0.37	(0.02)	0.12	(0.00)	99.66	(0.16)	82.50	(0.23)
P-2007-19a	8	4	39.39	(0.02)	43.32	(0.08)	16.40	(0.06)	0.38	(0.01)	0.12	(0.00)	99.61	(0.11)	82.48	(0.06)
P-2007-19a	9	4	39.24	(0.08)	43.39	(0.22)	16.92	(0.40)	0.32	(0.04)	0.13	(0.00)	100.01	(0.14)	82.05	(0.42)
P-2007-19a	10	4	39.35	(0.10)	43.37	(0.30)	16.87	(0.29)	0.35	(0.03)	0.12	(0.00)	100.07	(0.14)	82.09	(0.35)
Mean			39.07	(0.22)	43.94	(0.51)	15.46	(0.40)	0.38	(0.05)	0.12	(0.01)	98.96	(0.59)	83.51	(0.44)

(continued on next page)

Please cite this article as: Erlund, E.J., et al., Compositional evolution of magma from Parícutin Volcano, Mexico: The tephra record, Journal of Volcanology and Geothermal Research (2009), doi:10.1016/j.jvolgeores.2009.09.015

Appendix Table 3 (*continued*)

Sample	Olivine	*n*	SiO_2	1σ	MgO	1σ	FeO	1σ	NiO	1σ	CaO	1σ	Total	1σ	Fo(%)	1σ
P-2007-3a	1	4	39.10	(0.07)	43.08	(0.47)	15.23	(0.82)	0.40	(0.08)	0.12	(0.01)	97.91	(0.44)	83.45	(0.88)
P-2007-3a	2	4	39.04	(0.25)	43.70	(0.42)	15.53	(0.22)	0.34	(0.03)	0.13	(0.01)	98.74	(0.71)	83.38	(0.20)
P-2007-3a	3	4	38.94	(0.05)	43.99	(0.22)	14.95	(0.12)	0.43	(0.02)	0.12	(0.01)	98.43	(0.28)	83.99	(0.13)
P-2007-3a	4	4	38.86	(0.09)	43.88	(0.19)	15.25	(0.12)	0.40	(0.01)	0.12	(0.01)	98.51	(0.23)	83.69	(0.14)
P-2007-3a	5	4	38.93	(0.03)	44.50	(0.04)	15.29	(0.08)	0.41	(0.02)	0.11	(0.00)	99.25	(0.08)	83.84	(0.08)
P-2007-3a	6	4	38.86	(0.08)	44.48	(0.14)	15.40	(0.15)	0.42	(0.02)	0.12	(0.00)	99.27	(0.22)	83.73	(0.17)
P-2007-3a	7	4	38.95	(0.12)	43.76	(0.43)	15.69	(0.49)	0.34	(0.04)	0.13	(0.00)	98.87	(0.17)	83.26	(0.57)
P-2007-3a	8	4	39.36	(0.11)	43.78	(0.48)	15.66	(0.63)	0.37	(0.06)	0.12	(0.01)	99.30	(0.20)	83.28	(0.71)
P-2007-3a	9	4	39.53	(0.07)	44.73	(0.12)	15.20	(0.05)	0.38	(0.03)	0.13	(0.00)	99.97	(0.21)	83.99	(0.03)
P-2007-3a	10	4	39.09	(0.06)	43.45	(0.24)	16.39	(0.33)	0.28	(0.04)	0.13	(0.01)	99.34	(0.23)	82.54	(0.36)
Mean			39.07	(0.22)	43.94	(0.51)	15.46	(0.40)	0.38	(0.05)	0.12	(0.01)	98.96	(0.59)	83.51	(0.44)
P-2007-6a	1	4	39.26	(0.12)	44.76	(0.28)	14.72	(0.07)	0.41	(0.01)	0.12	(0.00)	99.26	(0.20)	84.43	(0.14)
P-2007-6a	2	4	39.34	(0.15)	44.45	(0.47)	14.93	(0.31)	0.40	(0.04)	0.12	(0.01)	99.24	(0.37)	84.14	(0.41)
P-2007-6a	3	4	39.31	(0.03)	44.54	(0.33)	14.69	(0.10)	0.41	(0.01)	0.12	(0.00)	99.07	(0.36)	84.39	(0.12)
P-2007-6a	4	4	39.35	(0.09)	44.47	(0.15)	14.55	(0.08)	0.41	(0.02)	0.12	(0.01)	98.90	(0.25)	84.49	(0.07)
P-2007-6a	5	4	39.22	(0.11)	44.83	(0.12)	14.69	(0.09)	0.40	(0.02)	0.12	(0.00)	99.26	(0.16)	84.47	(0.11)
P-2007-6a	6	4	39.24	(0.08)	44.44	(0.21)	14.68	(0.22)	0.39	(0.01)	0.12	(0.01)	98.86	(0.09)	84.37	(0.26)
P-2007-6a	7	4	39.39	(0.03)	44.81	(0.11)	14.76	(0.05)	0.41	(0.02)	0.12	(0.01)	99.50	(0.19)	84.40	(0.02)
P-2007-6a	8	4	39.42	(0.07)	44.52	(0.09)	14.62	(0.12)	0.40	(0.01)	0.12	(0.01)	99.08	(0.13)	84.44	(0.13)
P-2007-6a	9	4	39.24	(0.10)	44.51	(0.20)	15.06	(0.21)	0.37	(0.02)	0.12	(0.01)	99.31	(0.30)	84.05	(0.21)
P-2007-6a	10	4	39.39	(0.04)	44.57	(0.05)	14.64	(0.12)	0.42	(0.02)	0.12	(0.00)	99.14	(0.11)	84.44	(0.11)
Mean			39.07	(0.22)	43.94	(0.51)	15.46	(0.40)	0.38	(0.05)	0.12	(0.01)	98.96	(0.59)	83.51	(0.44)
P-2007-9b	1	4	39.78	(0.03)	45.70	(0.04)	12.52	(0.07)	0.46	(0.02)	0.12	(0.00)	98.58	(0.03)	86.68	(0.07)
P-2007-9b	2	4	40.00	(0.17)	45.37	(0.41)	13.51	(0.55)	0.33	(0.07)	0.13	(0.00)	99.34	(0.14)	85.68	(0.60)
P-2007-9b	3	4	39.92	(0.06)	45.00	(0.08)	13.27	(0.17)	0.35	(0.02)	0.13	(0.01)	98.67	(0.25)	85.81	(0.15)
P-2007-9b	4	4	40.15	(0.06)	45.99	(0.19)	12.69	(0.18)	0.44	(0.02)	0.12	(0.00)	99.40	(0.14)	86.59	(0.21)
P-2007-9b	5	4	40.23	(0.05)	46.26	(0.04)	12.77	(0.09)	0.44	(0.01)	0.12	(0.01)	99.81	(0.14)	86.59	(0.08)
P-2007-9b	6	4	39.89	(0.44)	44.53	(1.91)	14.50	(2.31)	0.29	(0.11)	0.13	(0.00)	99.33	(0.22)	84.53	(2.64)
P-2007-9b	7	4	40.05	(0.13)	45.55	(0.49)	13.89	(0.70)	0.32	(0.06)	0.12	(0.01)	99.93	(0.23)	85.39	(0.75)
P-2007-9b	8	4	40.33	(0.10)	46.47	(0.12)	12.65	(0.06)	0.46	(0.01)	0.12	(0.01)	100.02	(0.23)	86.75	(0.03)
P-2007-9b	9	4	40.00	(0.06)	45.44	(0.05)	13.46	(0.05)	0.35	(0.02)	0.12	(0.01)	99.38	(0.07)	85.75	(0.06)
P-2007-9b	10	4	39.60	(0.25)	44.43	(1.13)	14.88	(1.45)	0.24	(0.08)	0.13	(0.01)	99.27	(0.04)	84.17	(1.64)
Mean			39.07	(0.22)	43.94	(0.51)	15.46	(0.40)	0.38	(0.05)	0.12	(0.01)	98.96	(0.59)	83.51	(0.44)

Values in parentheses are 1 standard deviation uncertainties based on replicate point analyses.

Please cite this article as: Erlund, E.J., et al., Compositional evolution of magma from Parícutin Volcano, Mexico: The tephra record, Journal of Volcanology and Geothermal Research (2009), doi:10.1016/j.jvolgeores.2009.09.015

References

Bannister, V., Roeder, P., Poustovetov, A., 1998. Chromite in the Parícutin lava flows (1943–1952). Journal of Volcanology and Geothermal Research 87, 151–171.

Blundy, J., Cashman, K., 2008. Petrologic reconstruction of magmatic system variables and processes. In: Minerals Inclusions and Volcanic Processes. Reviews in Mineralogy and Geochemistry 69, 179–239.

Blundy, J., Cashman, K., Humphreys, M., 2006. Magma heating by decompression-driven crystallization beneath andesite volcanoes. Nature 443, 76–80.

Cashman, K.V., Thornber, C.R., Kauahikaua, J.P., 1999. Cooling and crystallization of lava in open channels, and the transition of Pahoehoe Lava to `a`a. Bulletin of Volcanology 61, 306–323.

Cervantes, P., Wallace, P., 2003a. Magma degassing and basaltic eruption styles: a case study of 2000 year BP Xitle volcano in central Mexico. Journal of Volcanology and Geothermal Research 120, 249–270.

Cervantes, P., Wallace, P., 2003b. Role of H_2O in subduction-zone magmatism: new insights from melt inclusions in high-Mg basalts from central Mexico. Geology 31, 235–238.

Dungan, M.A., 2005. Partial melting at the earth's surface: implications for assimilation rates and mechanisms in subvolcanic intrusions. Journal of Volcanology and Geothermal Research 140, 193–203.

Edwards, B.R., Russell, J.K., 1998. Time scales of magmatic processes: new insights from dynamic models for magmatic assimilation. Geology 26, 1103–1106.

Eggler, D.H., 1972. Water-saturated and undersaturated melting relations in a Paricutin andesite and an estimate of water content in the natural magma. Contributions to Mineralogy and Petrology 34, 261–271.

Foshag, W.F., González-Reyna, J., 1956. Birth and development of Parícutin volcano Mexico. Geological Survey Bulletin 965, 355–489.

Fries, C.J., 1953. Volumes and weights of pyroclastic material, lava, and water erupted by Paricutin volcano, Michoacan, Mexico. American Geophysical Union Transactions 34, 603–616.

Gaffney, E.S., Damjanac, B., Valentine, G.A., 2007. Localization of volcanic activity: 2. Effects of pre-existing structure. Earth and Planetary Science Letters 263, 323–338.

Hasenaka, T., 1994. Size, distribution, and magma output rate for shield volcanoes of the Michoacán-Guanajuato volcanic field, Central Mexico. Journal of Volcanology and Geothermal Research 63, 13–31.

Hasenaka, T., Carmichael, I., 1987. The cinder cones of Michoacán-Guanajuato Central Mexico: petrology and chemistry. Journal of Petrology 28, 241–269.

Hasenaka, T., Carmichael, I.S.E., 1985a. A complication of location, size and geomorphological parameters of volcanoes of the Michoacán Guanajuato Volcanic Field, Central Mexico. Geofisica International 24, 577–607.

Hasenaka, T., Carmichael, I.S.E., 1985b. The cinder cones of Michoacan-Guanajuato central Mexico: their age, volume and distribution, and magma discharge rate. Journal of Volcanology and Geothermal Research 25, 105–124.

Hasenaka, T., Masao, B., Delgado Granados, H., 1994. Contrasting volcanism in the Michoacan-Guanajuato Volcanic Field, central Mexico: shield volcanoes vs. cinder cones. Geofisica International 33, 125–138.

Heiken, G., 1978. Characteristics of tephra from cinder cone, Lassen Volcanic National Park, California. Bulletin of Volcanology 41, 119–130.

Johnson, D.M., Hooper, P.R., Conrey, R.M., 1999. XRF analysis of rocks and minerals for major and trace elements on a single low dilution li-tetraborate fused bead. Advances in X-ray analysis 41, 843–867.

Johnson, E.R., Wallace, P.J., Cashman, K.V., Delgado Granados, H., Kent, A., 2008. Magmatic volatile contents and degassing-induced crystallization at Volcán Jorullo, Mexico: implications for melt evolution and the plumbing systems of monogenetic volcanoes. Earth and Planetary Science Letters 269, 477–486.

Johnson, E.R., Wallace, P.J., Delgado Granados, H., Manea, V.C., Kent, A.J.R., Bindeman, I.N., Donegan, C.S., in press. Subduction-related volatile recycling and magma generation beneath central Mexico: Insights from melt inclusions, oxygen isotopes and geodynamic models. Journal of Petrology. doi:10.1093/petrology/egp051.

Johnson, E.R., Wallace, P.J., Cashman, K.V., Delgado Granados, H., this volume. Degassing of volatiles (H_2O, CO_2, S, Cl) during ascent, crystallization, and eruption of basaltic magmas. Journal of Volcanology and Geothermal Research.

Krauskopf, K., 1948. Mechanism of eruption at Parícutin Volcano, Mexico. Bulletin of the Geological Society of America 59, 711–732.

Krauskopf, K., Williams, H., 1946. The activity of Paricutin during its third year. American Geophysical Union Transactions 27, 406–410.

Luhr, J.F., 2001. Glass inclusions and melt volatile contents at Paricutin Volcano, Mexico. Contributions to Mineralogy and Petrology 142, 261–283.

Luhr, J., Carmichael, I., 1985. Jorullo Volcano, Michoacán, Mexico (1759–1774): the earliest stages of fractionation in calc-alkaline magmas. Contributions to Mineralogy and Petrology 90 (2), 142–161.

Luhr, J.F., Simkin, T., 1993. Paricutín: The Volcano Born in a Mexican Cornfield. Geoscience Press, Inc., Phoenix, Arizona.

Luhr, J.F., Housh, T.B., 1993. A possible parental basalt to the Parícutin suite: the "early bomb" of Anguiano and Martinez. Eos Transactions of the American Geophysical Union 74 (43), 673.

Macdonald, G.A., 1972. Volcanoes. Prentice-Hall inc., Englewood Cliffs, New Jersey. 510 pp.

Martin, U., Nemeth, K., 2006. How Strombolian is a "Strombolian" scoria cone? Some irregularities in scoria cone architecture from the Transmexican Volcanic Belt, near Volcan Ceboruco (Mexico) and Al Haruj (Libya). Journal of Volcanology and Geothermal Research 155, 104–118.

McBirney, A.R., Taylor, H.P., Armstrong, R.L., 1987. Parícutin re-examined: a classic example of crustal assimilation in a calc-alkaline magma. Contributions to Mineralogy and Petrology 95, 4–20.

McKnight, S.B., Williams, S.N., 1997. Old cinder cone or young composite volcano?: The nature of Cerro Negro, Nicaragua. Geology 25, 39–342.

Moore, G., Carmichael, I.S.E., 1998. The hydrous phase equilibria (to 3 kbar) of an andesite and basaltic andesite from western Mexico: constraints on water content and conditions of phenocryst growth. Contributions to Mineralogy and Petrology 130, 304–319.

Nicholis, M.G., Rutherford, M.J., 2004. Experimental constraints on magma ascent rate for the Crater Flat volcanic zone hawaiite. Geology 32, 489–492.

Ownby, S.Delgado, Granados, H., Lange, R.A., 2007. Volcan Tancitaro, Michoacan, Mexico: $^{40}Ar/^{39}Ar$ constraints on its history of sector collapse. Journal of Volcanology and Geothermal Research 161, 1–14.

Pioli, L., Erlund, E., Johnson, E., Cashman, K., Wallace, P., Rosi, M., Delgado Granados, H., 2008. Explosive dynamics of violent strombolian eruptions: the eruption of Parícutin volcano 1943–1952 (Mexico). Earth and Planetary Science Letters 271, 359–368.

Pioli, L., Cashman, K., Azzopardi, B.J., 2009. Controls on the explosivity of scoria cone eruptions: magma segregation at conduit junctions. Journal of Volcanology and Geothermal Research. doi:10.1016/j.jvolgeores.2009.07.014.

Roggensack, K., Hervig, R.L., McKnight, S.B., Williams, S.N., 1997. Explosive basaltic volcanism from Cerro Negro volcano: influence of volatiles on eruptive style. Science 277, 1639–1642.

Scandone, R., 1979. Effusion rate and energy balance of Paricutin eruption (1943–1952), Michoacan, Mexico. Journal of Volcanology and Geothermal Research 6, 49–60.

Segerstrom K., 1950. Erosion studies at Paricutín. United States Geological Survey Bulletin, 164.

Spilliaert N., Allard P., Metrich N., Sobolev A.V., 2006. Melt inclusion record of the conditions of ascent, degassing, and extrusion of volatile-rich alkali basalt during the powerful 2002 flank eruption of Mount Etna (Italy). Journal of Geophysical Research-Solid Earth 111(B04203). doi:10.1029/2005JB003934.

Strong, M., Wolff, J., 2003. Compositional variations within scoria cones. Geology 31, 143–146.

Taddeucci, J., Pompilio, M., Scarlato, M., 2004. Conduit processes during the July–August 2001 explosive activity of Mt. Etna (Italy): inferences from glass chemistry and crystal size distribution of ash particles. Journal of Volcanology and Geothermal Research 137, 33–54.

Toplis, M.J., 2005. The thermodynamics of iron and magnesium partitioning between olivine and liquid: criteria for assessing and predicting equilibrium in natural and experimental systems. Contributions to Mineralogy and Petrology 149, 22–39.

Valentine, G.A., Krogh, K.E.C., 2006. Emplacement of shallow dikes and sills beneath a small basaltic volcanic center—the role of pre-existing structure (Paiute Ridge, southern Nevada, USA). Earth and Planetary Science Letters 246, 217–230.

Valentine, G., Gregg, T., 2008. Continental basaltic volcanoes—processes and problems. Jounral of Volcanology and Geothermal Research 177, 857–873.

Valentine, G.A., Krier, D., Perry, F.V., Heiken, G., 2005. Scoria cone construction mechanisms, Lathrop Wells volcano, southern Nevada, USA. Geology 33, 629–632.

Valentine, G.A., Perry, F.V., a Krier, D., Keating, G.N., Kelley, R.E., Cogbill, A.H., 2006. Small-volume basaltic volcanoes: eruptive products and processes, and posteruptive geomorphic evolution in Crater Flat (Pleistocene), southern Nevada. GSA Bulletin 118, 1313–1330.

Valentine, G.A., Krier, D.J., Perry, F.V., Heiken, G., 2007. Eruptive and geomorphic processes at the Lathrop Wells scoria cone volcano. Journal of Volcanology and Geothermal Research 161, 57–80.

Walker, G.P.L., 1973. Explosive volcanic eruptions—a new classification scheme. Geologische Rundschau 62, 431–446.

Wilcox, R.E., 1954. Petrology of Paricutín volcano Mexico. Geological Survey Bulletin 965 (C), 281–353.

Yokoyama, I., de la Cruz-Reyna, S., 1990. Precursory earthquakes of the 1943 eruption of Parícutin volcano, Michoacan, Mexico. Journal of Volcanology and Geothermal Research 44, 265–281.

Please cite this article as: Erlund, E.J., et al., Compositional evolution of magma from Parícutin Volcano, Mexico: The tephra record, Journal of Volcanology and Geothermal Research (2009), doi:10.1016/j.jvolgeores.2009.09.015